Origin of Antecrysts in Igneous Rocks from the Salavat Range (NW Iran): an Explanation for the Geochemical Signature of Potassic Alkaline Rocks

Azam Soltanmohammadi, Michel Grégoire, Georges Ceuleneer, Mathieu Benoit, L Paul Bédard, Sophie Gouy, Michel Rabinowicz

Origin of antecrysts in igneous rocks from the Salavat Range (NW Iran): an explanation for the geochemical signature of potassic alkaline rocks

Azam Soltanmohammadi[1,2]*, Michel Grégoire[1], Georges Ceuleneer[1], Mathieu Benoit[1], L.Paul Bédard[2], Sophie Gouy[1,3] and Michel Rabinowicz[1]

[1] Géosciences Environnement Toulouse (GET), Observatoire Midi-Pyrénées, Université Paul Sabatier Toulouse III-CNRS-CNES-IRD, Toulouse, France; [2] Centre d'étude sur les Ressources minérales (CERM), Sciences de la Terre & LabMaTer, Université du Québec à Chicoutimi, Chicoutimi, Québec, Canada; [3] UMS 3623 -Centre de MicroCaractérisation Raimond Castaing Université Paul Sabatier Toulouse III-CNRS, Toulouse, France

*Corresponding author. E-mail: azamsoltanmohammadi@gmail.com

ABSTRACT

Abundant silica-undersaturated potassic lavas are found in the centre of the Turkish-Iranian plateau (NW Iran) as flows, pillows and dykes. They display abundant zoned clinopyroxene macrocrysts and xenoliths of igneous cumulates. We determined four types of zoned crystals (Type-I, -II, -III and -IV) on the basis of their composition and zoning patterns. Use of in situ compositional data, together with whole-rock major and trace elements and the isotopic signatures of the host lavas provided evidence for the derivation of the different types of zoned clinopyroxenes from at least two contrasting parental melts. Our findings are consistent with an origin of the ultrapotassic and sodic alkaline melts from the deep-seated compaction pockets inferred from our previous studies of the alkaline magmatism throughout the Turkish-Iranian plateau. The ultrapotassic melt, which accumulated at the top of the compaction pockets, eventually ponded close to the spinel–garnet mantle transition and generated colourless antecrysts (Type-I and Type-II) and clinopyroxenite

cumulates. When the compaction pocket impinged on the continental lithosphere, interstitial melts segregated and flowed inside dykes where grass green antecrysts (Type-III) and zoned phenocrysts (Type-IVa) crystallized from a melt having a geochemical signature of sodic alkaline melt. Later, at the crustal level, melt crystallization processes produced Type-IVb zoned phenocrysts. Our results are at odds with the paradigm of potassic magmas in NW Iran being derived strictly from a single mantle source.

KEYWORDS: potassic alkaline rocks, zoned clinopyroxene, mixing, antecrysts, cumulates, Turkish-Iranian plateau, compaction pocket

INTRODUCTION

Multiple experiment-based and natural sample–based studies of alkaline magmatism document that the broad composition (ultrapotassic to sodic series) of these melts originates from the partial melting of metasomatized upper mantle sources (e.g. Foley, 1992). Under favourable conditions, these melts may pond and collect within magma reservoirs at either the lithospheric level, crustal level or both (e.g. Rigo *et al.*, 2015). In these settings, the melts begin to cool and crystallize before ascending and erupting at the surface. Accordingly, the chemical composition of alkaline melts could evolve from either a single process or a combination of processes that include (i) modification during mineral crystallization (Larrea *et al.*, 2012; Ubide *et al.*, 2014; Jankovics *et al.*, 2016); (ii) a mixing with other mantle-derived melt(s) or the assimilation of mantle-derived crystals or rocks (Muravyeva *et al.*, 2014); and (iii) the assimilation of or the contamination by crustal components (Conticelli, 1998; Prelević *et al.*, 2004; Zhu & Ogasawara, 2004; Jankovics *et al.*, 2016).

Strikingly different zoning patterns—concentric normal, reverse, oscillatory or a combination of these patterns—are commonly recorded in alkaline lavas. Zoned macrocrysts of clinopyroxenes, testifying to open-system processes during magmatic evolution, provide some of

the best evidence of magma mixing (e.g. Ginibre *et al*., 2007; Streck, 2008). Some zoning features (e.g. oscillatory-sectored zoning), however, have been interpreted as evidence of crystallization kinetics (e.g. Ubide *et al*., 2019). In orthopyroxene-free alkali olivine basalts and potassium-rich alkaline magmas, the major mafic phase contains colourless to green clinopyroxene of a near-diopside or salite composition (e.g. Mitchell, 1995b). Among potassium-rich alkaline rocks from the Mediterranean region, the mineral chemistry of these clinopyroxenes has been reported for the Catalonian Coastal Range (Ubide *et al*., 2014), Corsica (Wagner & Velde, 1986), central and southern Italy (e.g. Barton *et al*., 1982; Conticelli, 1998; Perini & Conticelli, 2002) as well as west and central Anatolia (Semiz *et al*., 2012; Grützner *et al*., 2013). Alkaline rocks from the French Massif Central (Pilet *et al*., 2002), Eifel (e.g. Duda & Schmincke, 1985) and the Pannonian Basin (e.g. Jankovics *et al*., 2016) also contain similar clinopyroxene crystals. The compositional gap observed between the colourless and green zones has been interpreted as them originating from different melts derived from a single or multiple sources (Tappe, 2004; Orejana *et al*., 2007; Larrea *et al*., 2012; Grützner *et al*., 2013). In the case of a single source, suggested processes include (i) fractional crystallization from a single melt, although at differing pressures, f_{H2O} or f_{O2}, cooling rates and crystal growth (Barton *et al*., 1982 references therein; Orejana *et al*., 2007); (ii) the mixing of various melt compositions related to differing degrees of melting of a single source (Tappe, 2004); and (iii) thermal or chemical convection (or both) in a magma chamber (e.g. Couch *et al*., 2001). In many cases, however, the link between mineral-scale zoning patterns and whole-rock geochemical data remains poorly developed. Accordingly, the occurrence of zoned clinopyroxenes hosted within potassic alkaline lavas invokes a central question: Is the potassic affinity of melt a primary characteristic? An answer to this question is important as natural sample and experimental studies rely on the main characteristics of alkaline rocks to serve as fundamental tools for speculating on the nature of mantle sources.

The uncertainty surrounding the origin of potassic magmatism and its widespread occurrence in orogenic systems has motivated multiple investigations. These studies describe numerous silica-undersaturated to silica-oversaturated potassium-rich lavas (shoshonites, lamprophyres, lamproites, leucite-bearing lavas) from the Alpine-Himalaya orogenic belt (Barton *et al*., 1982; Wagner & Velde, 1986; Perini & Conticelli, 2002; 2015; Pang *et al*., 2013; Aghazadeh *et al*., 2015). In general, these studies propose that the potassic affinity of a melt is a primary characteristic derived from heterogeneous mantle sources located at shallow depths. Such heterogeneity of mantle sources involves either (i) a subducting oceanic slab (Wang & Foley, 2018) or (ii) a partial melting process of a K-bearing subcontinental lithospheric mantle (Foley, 1992; Condamine & Médard, 2014; Condamine *et al*., 2016; Förster *et al*., 2016). These melts could be eventually contaminated by continental crust, producing features that are sometimes opposite to those generally associated with the crustal contamination of other types of mafic melts (e.g. Conticelli, 1998; Prelević *et al*., 2004). The nature of mantle sources able to explain both the silica undersaturation and the potassic affinity of the melts remains nonetheless enigmatic.

A large volume of potassic alkaline magmatic rocks occurs within the Turkish-Iranian plateau. Except for a few studies (e.g. Semiz *et al.,* 2012; Prelević *et al*., 2015), previous works focused mainly on whole-rock composition to determine the origin of these magmatic rocks. Thus, these studies did not address the great diversity of zoning features in clinopyroxenes and their potential use for interpreting whole-rock geochemical data. Here, we report for the first time, major and trace element compositions of various zoned patterns of clinopyroxenes that occur in alkaline volcanic rocks from NW Iran (Salavat Range). We combine the mineral modal abundance and chemistry of these clinopyroxenes with whole-rock major and trace elements, as well as Nd–Sr isotopic features, to investigate how zoned patterns in the clinopyroxene macrocrysts are reflected

by whole-rock geochemistry. In particular, we consider the implication of compaction pockets as proposed by Soltanmohammadi *et al.* (2018). According to this model, the origin of various highly ultrapotassic and sodic alkaline rocks from the Turkish-Iranian plateau could be derived from multiple stages of melt-extraction events. These events follow the ascent of compaction pockets, originating from the mantle transition zone, through the entire upper mantle (Soltanmohammadi *et al.* 2018). We highlight that a highly precise assessment of mineral composition is required to determine whether the potassic affinity of melts represents an initial (primary) characteristic of a melt or is attributable to mixing processes between two endmembers—ultrapotassic and sodic—derived from different mantle sources.

REGIONAL GEOLOGY

The geological features of the Turkish-Iranian plateau relate to processes associated with the Tethys subduction and the subsequent collision between the Eurasian and Arabian plates along the 2400-km-long Bitlis–Zagros suture zone (Stampfli, 2000). The Arabia-Eurasia collision occurred between the Late Cretaceous and Late Miocene (Stampfli, 2000). The precise chronology remains debated because of the geological complexity of the area. Widespread continental magmatism covered over half of the Turkish-Iranian plateau surface during four magmatic periods: (i) Jurassic–Cretaceous, (ii) Late Cretaceous–Palaeocene, (iii) Early–Middle Cenozoic and (iv) Late Cenozoic to the present. The Jurassic–Cretaceous magmatic period consists mostly of calc-alkaline magmatic intrusions (e.g. Hassanzadeh & Wernicke, 2016), whereas the magmatism is essentially alkaline from the Late Cretaceous onward (Pearce *et al.*, 1990; Vincent *et al.*, 2005; Castro *et al.*, 2013; Pang *et al.*, 2013; Aghazadeh *et al.*, 2015; Prelević *et al.*, 2015).

The East Anatolia–NW Iran–South Armenia Block is the largest region of the Turkish-Iranian plateau that is covered by Cenozoic–Quaternary magmatism (Pearce *et al.*, 1990). In NW

Iran, multiphase magmatic activities formed the Azerbaijan magmatic zone (AMZ in Fig. 1a), which is marked by a high volume of Cenozoic alkaline magmatism (Alberti *et al.*, 1976; Aghazadeh *et al.,* 2015). However, Pliocene–Quaternary eruptions produced both alkaline lava flows and cinders (Sabalan Volcano in Fig. 1a) of calc-alkaline composition and adakitic affinity. South of the Azerbaijan magmatic zone, the Oligo–Miocene to Quaternary alkaline magmatic provinces are separated from the Arabian foreland by the Zagros suture (e.g. Pang *et al.*, 2013). To the north, the Azerbaijan magmatic zone is covered extensively by Early Cretaceous–Neogene volcano-sedimentary successions (6300 km^2) extending to the Lesser Caucasus, the Armenia Block and the Alborz (Vincent *et al.*, 2005). East of the Azerbaijan magmatic zone, Vincent *et al.* (2005) described an equivalent of the Lesser Caucasus volcano-sedimentary succession (Talesh in Fig. 1a), where lavas are high-K calc-alkaline to potassic alkaline rocks. Toward the central–western portion of the Alborz, Eocene magmatism is mainly high-K calc-alkaline to potassic lavas with pyroclastic deposits and intrusions (Castro *et al.,* 2013).

In the central part of the Azerbaijan magmatic zone, Eocene magmato-sedimentary sequences crop out over approximately 1500 km^2, an area known as the Salavat Range (Fig. 1b; Babakhani *et al.,* 1990). The main magmatic lithologies in this range consist of pyroclastic deposits, lava flows and swarms of dykes. In the following paragraphs, we detail these elements.

Volcanic breccia and pillow lavas: They are the primary lithologies covering the Salavat Range. Volcanic breccias (Fig. 2a) crop out with volcanic fragments ranging 50–200 mm in diameter, whereas outcrops of pillow lavas are marked by mega pillow basalt (1–5 m) features (Fig. 2b).

Dykes: These intrusions represent unique planar magmatic structures not only in the Salavat Range but also across the entire Iranian plateau. Dykes cluster around the central and eastern parts of the Salavat Range, and they disappear abruptly along the range's western and southern edges. The dykes cross-cut the volcanic breccias as swarms of dykes that vary in length, orientation and lithology. Two very different sets of dykes are present. Dykes of the first set contain horizontal columnar joint structures (Fig. 2c) and are related to Middle–Late Eocene magmatic events (42.7–38.4 Ma, Alberti *et al.*, 1976). This set of dykes cross-cuts both the second set and the volcanic breccia (e.g. Fig. 2d). Dykes of the second set are thus older than the first set and lack distinctive features. Mafic and ultramafic cumulates—ranging from a few centimetres to more than 10–20 cm in size—are commonly dark green, irregularly shaped inclusions within these dykes (Fig. 2e and f).

Analcimite and analcime-bearing lavas: The abundance of subaerial analcime-bearing lavas and pyroclastic deposits is noteworthy in the Salavat Range (Comin-Chiaramonti *et al.,* 1979). Columnar joint structure in these lavas occurs as radial and perpendicular structures (Fig. 2g). Stratigraphic relationships demonstrate that these deposits are younger than the volcanic breccia, pillow lavas and dykes (Babakhani *et al.,* 1990). The lavas are covered by Oligocene–Miocene clastic sandstones and conglomerate sediments (Fig. 2h). The radiometric age of these lavas has not been determined. To the south of the Azerbaijan magmatic zone, similar lavas and pyroclastic deposits extend ~100 km (to the Bozkush Mountains). These lavas are products of Eocene–Oligocene volcanic eruptions (Lescuyer *et al.,* 1978).

ANALYTICAL METHODS

We selected 33 samples to measure major elements by ICP-AES and trace element concentrations by high-resolution inductively coupled plasma mass spectrometer (HR-ICP-MS (Table 1) and 9

samples were analysed with a Finnigan MAT 261 to measure Nd–Sr radiogenic isotopes of whole rocks (Table 2). The main rock-forming minerals were selected to measure major elements (Supplementary Table S1). We also undertook a systematic in situ measurement of major and trace element distribution within the zoned clinopyroxenes (e.g. Tables S1 and S2). The details of our analytical methods for whole rocks and minerals are listed in the Supplementary Material: analytical methods.

RESULTS

Rock-type classification, petrography and mineral chemistry

Petrography and mineralogy

The porphyricity index (PI: total phenocryst vol%) of various stratigraphic units found in the Salavat Range is variable (Fig. S1). The lavas and dykes having a highly variable porphyricity index (7.7–50%) contain >1 mm crystals, whereas lavas having a more limited range of porphyricity index (e.g. 20%) generally have ≤1 mm crystals. To describe the porphyritic characteristics of samples, we used only the non-genetic terms of megacryst (>3 mm), macrocryst (1–3 mm) and microcryst-microlith (<1–0.5 mm). We also combined petrographic observations, mineral composition and whole-rock geochemistry to classify the different types of clinopyroxenes (Fig. 3a and b) and define the genetic terms of antecryst and phenocryst. We relied on the nature and abundance of the main minerals to divide the sampled rocks into clinopyroxene-plagioclase phyric basalts (volcanic breccias), clinopyroxene-phlogopite phyric basalt (dykes), analcime-clinopyroxene phyric basalts (dykes), analcime-bearing clinopyroxene phyric basalt (pillow lavas), analcime-phyric basalts (analcimite and analcime-bearing lavas) and a heterogeneous suite of

cumulative xenoliths that include clinopyroxenite, phlogopite-bearing clinopyroxenite and monzogabbro.

Clinopyroxene-plagioclase phyric basalts

Clinopyroxene is the main macrocryst phase (6 vol %) and is characterized by oscillatory and patchy zoning. Clinopyroxene ranges in composition and colour from a high Mg# ([Mg/(Mg+Fe^{2+})] >0.75), colourless diopside to a low Mg# (~<0.75), pale green diopside to fassaite. Locally, unzoned macrocrysts of diopside are set in a heterogenous magmatic texture (i.e. mingling; Fig. S2a). Plagioclase is the second-most abundant type of macrocryst (4 vol %) and is labradorite in composition ($Ab_{26.6–35.5}$ $An_{59.1–69.9}$ $Or_{3.3–5.2}$) with respective Na_2O and FeO contents of 3.02–3.9 wt % and 0.9–1.02 wt %.

Clinopyroxene-phlogopite phyric basalts (lamprophyres)

According to the classification for exotic magmatic rocks (e.g. Rock, 1977), the above-mentioned second set of dykes (i.e. the earliest dykes) has a lamprophyre nature that varies in composition from kersantite to minette. Both kersantite and minette are highly porphyritic (17.1–20.7% and 9.4–23.2%, respectively).

Minette. Clinopyroxene (15 vol %) and phlogopite (5 vol %) are the most abundant mafic macrocrysts. They are characterized by pale green oscillatory-zoned rims that mantle colourless cores (Fig. S2b). The abundance of colourless core megacrysts (10 vol %) of clinopyroxenes is marked relative to the abundance of clinopyroxene macrocrysts having only pale green oscillatory zoning (5 vol %). Phlogopite ranges from megacryst to macrocryst in size (Fig. S2c). Evidence of disequilibrium between phlogopite megacrysts and the surrounding melt is evidenced by the partial

resorption of phlogopite and the development of the reaction rim of Fe-oxides (Fig. S2d). Phlogopites have a high Mg# (0.73–0.82) and Cr_2O_3 (0.06–0.6 wt %) with low TiO_2 (0.95–2.24 wt %) and Al_2O_3 (14.7–15.2 wt %). Sanidine ($Ab_{36.7–41.39}$ $An_{3.2–6.7}$ $Or_{52.7–59.3}$), as the sole feldspar, is the main groundmass mineral. It has a relatively high FeO content (0.34–0.55 wt %).

Kersantite. Similar to minette, megacrysts of clinopyroxene occur, albeit at a lower proportion (1–5 vol %). They vary between colourless diopside to grass green to pale green fassaite. Some zoned macro- to microcrysts of clinopyroxene occur (up to 4 vol %) and are characterized by a grass green core mantled by either colourless or pale green zones, a feature absent from minettes. Grass green zones, which occur either in the core or on the rim (Fig. S2e and f), are fassaite in composition and are relatively high in Na_2O and Al_2O_3 (Fig. 4). Amphibole (magnesio-hastingsite, Supplementary Table S1) and bytownite plagioclase ($Ab_{7.4–15.5}$ $An_{83.4–92.1}$ $Or_{0.2–1}$) also appear as microcrysts (up to 2 vol % and 8 vol %, respectively). In contrast to the minettes, biotite only appears as microcrysts. These microcrysts also differ in their composition from that of the biotite from minette (Supplementary Table S1), having a lower Mg# (0.63–0.79) and Cr_2O_3 (0–0.2 wt %) nd a higher TiO_2 (1.33–3.9 wt %) and Al_2O_3 (14.1–16.07 wt %) content. The mineral assemblage in the groundmass differs as well, as the kersantite groundmass consists mainly of microcrystalline clinopyroxene and biotite associated with variable amounts of feldspar and glass.

Analcime-clinopyroxene phyric basalts

Analcime-clinopyroxene phyric basalts have a high and variable porphyricity index (8–50%) with mega- to macrocrysts set in a fine-grained holocrystalline groundmass. These basalts are found in the first set of dykes and are composed mainly of analcime (2–23 vol %), clinopyroxene (5–10 vol

%) and plagioclase (up to 11 vol %) macrocrysts with accessory apatite and magnetite. Rare olivine (Fo: 50–71) macrocrysts (<1 vol %) may occur and are characterized by disequilibrium embayment edges and CaO and MnO contents of 0.15–0.41 wt % and 0.58–0.79 wt %, respectively. Most clinopyroxene macrocrysts (2–3 vol %) are pale green oscillatory- zoned; their composition evolves from diopside toward fassaitic (Fig. 4a). However, high Mg# (0.75–0.88) colourless diopsides (2–4 vol %) also occur as mega- to macrocrysts. Here and there, colourless zones appear as bright narrow bands (Fig. 5a–e) located in between pale green oscillatory-zoned parts in macrocrysts (<2 vol %); the colourless zones have a high Na_2O content (up to 0.8 wt %; Fig. 5f). Analcime macrocrysts appear mainly as polyhedral macrocrysts (3–18 vol %) and contain K_2O (0.04–0.13 wt %). Plagioclase, as macrocrysts (up to 11 vol %), varies in composition from labradorite ($An_{50.6–70.8}$ $Ab_{27.1–42.08}$ $Or_{2.01–9.7}$) to sanidine ($An_{2.1–5-9}$ $Ab_{9.5–37}$ $Or_{58.6–95.36}$). The microcrystalline groundmass consists of the same minerals as the macrocryst suite, having apatite, magnetite and, in rare cases, needles of biotite.

Analcime-bearing clinopyroxene phyric basalts

Macrocrysts of euhedral grass green clinopyroxene (4–12 vol %) have a lower Mg# (~0.80–0.6) than the rock types described above and range in composition from diopside to fassaite. Analcime occurs mainly as microcrysts (3 vol %) and displays a low K_2O (0.02–0.04 wt %) content. We also observed clusters of clinopyroxene-plagioclase (5–7 vol %) as glomerophenocrysts set in a groundmass, which was marked by quenched clinopyroxenes and swallow-tailed plagioclases (Fig. S2g).

Analcime-phyric basalts

Similar to analcime-bearing clinopyroxene phyric basalts, analcime-phyric basalts have porphyritic, hyalomicroporphyritic and glomeroporphyritic textures. In contrast, the latter basalts have a higher and lower volume proportion of euhedral analcime (10–15 vol %) and clinopyroxene (2–4 vol %), respectively. Euhedral analcime in the analcime-phyric basalts has a low K_2O content, similar to that of other analcime-bearing lavas (Table S1). As well, the analcime-phyric basalts contain inclusions of clinopyroxene, apatite and Fe-oxides along the crystal growth lines (Fig. S2i). Euhedral oscillatory-zoned clinopyroxenes are grass green macrocrysts. These macrocrysts have an evolved composition with a low Mg# (0.61–0.68) and SiO_2 (43.9–47.6 wt %), high TiO_2 (1.17–2.14 wt %), Al_2O_3 (6.5–9.4 wt %) and Na_2O (0.5–1.2 wt %), and they are fassaite in composition ($Wo_{51.87–56.19}$ $En_{32.2–37.8}$ $Fs_{7.4–11.6}$). Plagioclase occurs as a euhedral oscillatory-zoned macrocryst (2 vol %) that varies from bytownite ($An_{71.04–76.1}$ $Ab_{22.8–27.4}$ $Or_{0.7–1.5}$) to andesine ($An_{47.2}$ $Ab_{49.8}$ $Or_{2.8}$).

Cumulative xenoliths

Cumulate-I (clinopyroxenites) are nearly monomineralic (Fig. S2j) and consist of colourless, high Mg# (0.72–0.9) diopsides ($Wo_{48.3–51.6}$ $En_{38.4–46.6}$ $Fs_{1.6–9.4}$) with a relatively high Cr_2O_3 concentration (up to 0.5 wt %). At the contact between the cumulates and host lavas, the diopside can be strongly pleochroic and oscillatory-zoned with a low Mg# (0.60–0.75) and Cr_2O_3 (<0.08 wt %) and high TiO_2 (0.6–1.4 wt %) and Al_2O_3 (3.1–9.1 wt %) along the rim (Fig. 5g–l); alternatively, the diopside can also form clusters of crystals that include amphibole, feldspar and apatite.

Cumulate-II (mica-bearing clinopyroxenites) contain abundant clinopyroxene crystals (diopside to fassaite: $Wo_{49.2–54.6}$ $En_{37.2–44.2}$ $Fs_{4.05–11.4}$) and biotite as an intercumulus mineral (Fig.

S2k). In contrast to the clinopyroxenites, there is no zoning at the contact between these cumulates and host lavas. For major elements, clinopyroxenes have variable Mg# (0.71–0.86), Al_2O_3 (0.6–4.3 wt %) and Na_2O (0.08–0.5 wt %). Their composition overlaps partly with that of the grass green and colourless zones of kersantite clinopyroxenes (Supplementary Table S1). Its biotite has a similar composition to that of kersantite (Mg#: 0.66–0.76; TiO_2: 2.1–3.4 wt %; Al_2O_3: 14.4–16.04 wt %; Na_2O: ~0.3–0.7 wt %).

Cumulate-III (monzogabbros) are mineralogically similar to the plutonic rocks reported from the same region (see Soltanmohammadi, 2018 for details). Clinopyroxene is abundant and mainly fassaite in composition ($Wo_{47.3–52.3}$ $En_{36.1–44.5}$ $Fs_{6.7–14.9}$), having a narrow range of Mg# (0.68–0.77), Na_2O (0.28–0.83 wt %) and Al_2O_3 (0.9–5.5 wt %). It is similar in composition to the grass green zone of clinopyroxene within the kersantites (Supplementary Table S1). The feldspars are mainly andesine–labradorite ($An_{43.8–60.2}$ $Ab_{38.1–70.4}$ $Or_{1.5–7.7}$). Biotite has lower MgO (12.2–14.6 wt %), Al_2O_3 (14.1–15.1 wt %) and Na_2O (0.12–0.45 wt %), as well as higher TiO_2 (>3 wt %) than the mica-bearing pyroxenites.

Classification of zoned clinopyroxenes

Type-I: This type corresponds to zoned clinopyroxenes found as megacrysts in minette, kersantite or as mega- to microcrysts in analcime-clinopyroxene phyric basalts and clinopyroxenites (e.g. Fig. 5m–r). Overall, their zoning is “normal” (i.e. an increase in incompatible elements from the core to rim) and is characterized, in most cases, by an abrupt chemical change about halfway from the core to the rim (Mg# ~0.7; Fig. 5r). The colourless core has high Mg# and Cr_2O_3 but low Al_2O_3 and TiO_2. It is mantled by a pale green overgrowth having a low Mg# and Cr_2O_3 and high Al_2O_3 and TiO_2, as well as moderate Na_2O. For trace elements, the colourless cores

have negative Ba, Ta, Zr and Hf anomalies—although no Pb anomaly (Fig. S3)—whereas pale green rims display a similar pattern, albeit at higher concentrations. In terms of REEs, colourless cores have nearly parallel upward-convex patterns. These patterns are relatively flat for HREE and lack an Eu anomaly (Fig. 6).

Type-II: This type presents oscillatory zoning within pale green crystals and is marked by narrow bright bands. This type is observed only in analcime-clinopyroxene phyric basalts (tephrite dykes). The bright bands are distinguished by abrupt drops in Na_2O and relatively high Mg# and Cr_2O_3 (e.g. Fig. 5r). In terms of trace elements, the bright bands are depleted in Ba, Ta, Zr and Hf, with trace element contents well below those of the primitive mantle (Supplementary Fig. S3). For REEs, the bright bands have a distinctive pattern with a slightly higher LREE content and steeper HREE than the Type-I colourless zones (Fig. 6). They also contain higher concentrations of other incompatible elements (Sr, La, Nd, Zr and Hf), a slightly negative Pb anomaly and Nb–Ta decoupling.

Type-III: This type represents macrocryst grass green cores mantled either by colourless or pale green zones in kersantite. Given the melt evolution through the correlation of Na_2O, Al_2O_3 and Cr_2O_3 with Mg#, it appears that the core–rim trend records a reverse-zoned feature (Fig. 4b). Trace elements are characterized by a Nb–Ta decoupling and enriched REEs (×10–70). They display REE patterns having similar concave slopes, except for a slightly higher fractionation of LREE/HREE with a $(La/Yb)_N$ of 1.5–2.9.

Type-IV: This is the most abundant type of zoned macrocryst, occurring either in single-sectored, oscillatory-zoned crystals (Fig. 7) or at the contact between cumulative xenoliths and host lavas. Type-IV zoning patterns can be divided into two subtypes on the basis of their major element

content. The first subtype (Type-IVa) is observed only in analcime-bearing clinopyroxene phyric basalts (pillow lavas) and contains relatively high Na_2O (>0.4 wt %) and has a limited range of Mg# (~0.8–0.7). The second and most common subtype (Type-IVb) has a lower Na_2O (<0.4 wt %) and a more extensive Mg# range (0.8–0.6) (Fig. 8). Trace elements in Type-IVa are slightly enriched compared with those in Type-IVb. The $(La/Yb)_N$ of Type-IVa ranges from 1.5 to 4.7, and La content is ~10–75× higher than that of chondrite. Type-IVa zoning patterns are mostly transitional between the most depleted (Type-I) and most enriched (Type-III). They share similar characteristics with the other zoning types, such as having Nb–Ta decoupling. Slight drops in Pb and Zr–Hf pairs are highlighted by the normalized primitive mantle diagram (Fig. S3).

Whole-rock composition

Major elements

Alkaline magmatic rocks, such as kimberlites and lamproites, commonly have LOI values up to 10 wt % and have been studied for their whole-rock geochemical features (e.g. Becker & Le Roex, 2006). In our study, LOI values are locally high in the relatively primitive lavas, whereas the values are mostly high in evolved lavas. Accordingly, the correlation of alkali elements with LOI is mainly observed in the evolved lavas but not in primitive lavas. In this study, however, discussion of major and trace elements of primitive lavas is combined with in situ mineral chemistry and whole-rock radiogenic isotopes. As well, we did not include evolved lavas or the few primitive lavas having high LOI in our radiogenic studies or the discussion section. Note that our major element data are recalculated to 100% anhydrous.

Rock samples from volcanic breccia, dykes, pillow lavas and lava flows range from basanite through to phonotephrite and phonolite in composition (Fig. 9a). Concentrations of major elements

reveal that those lavas and dykes with the highest diversity of zoned crystals also have the greatest MgO content. In contrast, samples having a lower MgO content display only a single type of zoned crystal.

Most primary samples, volcanic breccias and the two types of dykes (lamprophyres and tephrites) are characterized by a low silica content (SiO_2: <50 wt %) and a high alkali content (K_2O+Na_2O: ~7–9 wt %). Samples plot mainly in the alkaline fields of the total alkali diagram (Fig. 9a). Volcanic breccias, lamprophyres and tephrites have a high content of MgO (7.8 wt %, 5.3–7.3 wt %, 4.3–6.1 wt %, respectively), Cr (380 ppm, 25–157 ppm, 27–76 ppm, respectively) and Ni (146 ppm, 15–60 ppm, 13–23 ppm, respectively). As well, all samples have high CaO (up to ~12 wt %) as well as low TiO_2 (<1 wt %) and Al_2O_3 (<18 wt %) contents. Volcanic breccias have a low SiO_2 content (49.6 wt %) and a high Na_2O+K_2O content (6.5 wt %)—these lavas plot in the tephrite–basanite field. The first set of dykes are characterized by a narrow compositional range (SiO_2: 48.2–50.6 wt %; Na_2O+K_2O: 6.7–7.9 wt %) and plot only in the tephrite–basanite field, whereas the dykes of the second set (lamprophyres), having variable SiO_2 (45.9–57.1 wt %) and total alkali (Na_2O+K_2O; 5.4–9.3 wt %) contents, display a wider range and fall within the basanite to tephrite to phono-tephrite fields (Fig. 9a). Lamprophyres may be classified as “calc-alkaline” on the basis of their petrography and mineral chemistry (see Rock, 1991); however, their whole-rock composition is characterized by low TiO_2 (0.71–0.96 wt %) and Al_2O_3 (13.8–17.3 wt %) contents with K_2O values of 1.45–5.15 wt %.

Pillow lavas and analcime-bearing lavas have relatively higher SiO_2 (>51.2 wt %), Al_2O_3 (up to ~22 wt %) and Na_2O (up to ~8 wt %) contents and a lower CaO (~<8 wt %) content than volcanic breccias and dykes; however, all these rocks share a similar TiO_2 content (<1 wt %). To define their alkaline affinity, we ruled out those lavas showing a positive correlation of LOI and Na_2O

contents. As shown in Figure 9b, the pillow lavas lie between the transitional to ultrapotassic fields; however, they have similar Na_2O values (>2 wt %) to the sodic lavas from the Turkish-Iranian plateau (>2.5 wt %), and their average K_2O content (>3 wt %) is higher than that of the sodic alkaline lavas from the plateau (<3 wt %).

Trace elements

Table 1 lists the trace element contents of representative samples from the different rock groups. Incompatible trace element characteristics are illustrated by primitive mantle and chondrite-normalized (Sun & McDonough, 1989) trace element and REE patterns (Fig. 9c and d). Although the various rock types differ in their respective major element concentrations, they all display trace element patterns characterized by enrichment in large-ion-lithophile elements (LILE; e.g. Rb, Th, U and Ba) relative to high-field-strength elements (HFSE; e.g. Nb, Ta and Ti). In general, the trace element content increases from more primitive lavas to the more evolved low MgO lavas. In high MgO lavas, the tephrite dykes display a substantial depletion in LILE (e.g. Sr, Th, U) and HFSE (Nb, Ta, Zr) compared with lamprophyres. REE patterns of all samples are characterized by a relatively high $(La/Yb)_N$ (6.3–24.1). The LREE/HREE ratios in some lithologies are rather uniform (e.g. tephrite dykes: La/Yb ~14–16; Table 1), whereas in lamprophyres—having the highest abundance and variety of zoned clinopyroxene—these values are quite heterogeneous (8–16). It is worth noting that most samples have an Eu/Eu* of ~0.7–0.9.

Nd–Sr isotopes

From the published geochronological data from our field area (Alberti *et al.*, 1976), we applied an age correction of 47 Ma (Table 2). The initial Sr and Nd isotopic compositions of samples from the Salavat Range are $^{143}Nd/^{144}Nd$ = 0.51259–0.51277 and $^{87}Sr/^{86}Sr$ = 0.70464–0.70593. All

samples plot within the mantle array (see later discussion), indicating the predominance of mantle sources; however, the Nd–Sr isotopic ratios from dykes have a moderately wide range. Lamprophyres display the most enriched isotopic signatures. The highest $^{87}Sr/^{86}Sr$ values (i.e. sample M-112; 0.70588), those of ultrapotassic–potassic rocks, were related previously to continental crust contamination processes or EM-II mantle sources (e.g. Weaver, 1991). In contrast, there is a limited range for pillow lavas ($^{143}Nd/^{144}Nd$: 0.51276–0.51277). Interestingly, those lamprophyres having high $^{143}Nd/^{144}Nd$ values (i.e. sample M-113; 0.51271) display similar values to those of pillow lavas, all scattering towards oceanic island basalt (OIB)–like mantle sources (Fig.10 a-d). Tephrite dykes, similar to lamprophyres, have scattered $^{143}Nd/^{144}Nd$ (0.51257–0.51265) and $^{87}Sr/^{86}Sr$ (0.70510–0.70541) values that lie between those of the ultrapotassic and sodic alkaline rocks from the Turkish-Iranian plateau.

DISCUSSION

Variations in whole-rock composition

Fractional crystallization

The extensive range of MgO concentrations (1.07–7.8 wt %) indicates that most studied samples are not representative of a primary melt that was in equilibrium with the mantle. Moreover, the positive correlation between CaO and SiO_2 and the negative correlation between TiO_2 and MgO (as well as the negative correlation between Al_2O_3 and MgO) imply that the crystal fractionation of feldspar and biotite does not play a critical role. In terms of trace element concentrations, the Eu anomaly (Eu/Eu*: 0.80–0.94) and the increase of Sr and Al_2O_3 with decreasing MgO demonstrate that the fractionation of plagioclase was insignificant in both lamprophyres and pillow lavas (e.g. Fig. S4). As we may see in Fig. S4, to explain the geochemical evolution from primitive lavas

(lamprophyre and tephrite dykes) to the evolved one a single fractional crystallization trend, relies on the composition with the higher MgO content. Moreover, the calculated fractional crystallization model cannot explain the scattered samples along the trend (e.g. Fig. S4e and f). The total modal abundance of the various types of clinopyroxene drops markedly with decreasing MgO (i.e. from volcanic breccias to analcimite lavas). We use a binary diagram to show the relationship between the modal abundance of the antecrysts and whole-rock chemistry. Fig.10 indicates the type of zoned clinopyroxene dominating the change in whole-rock alkali elements contents and radiogenic elements. For example, there is a positive correlation with the Na_2O content and $^{143}Nd/^{144}Nd$ ratio (Fig. 10b). Moreover, the modal abundance of grass green core crystal (Type-III), phenocryst in pillow lavas (Type-IVa) and colourless (Type-I and -II) antecrysts are correlated with the whole-rock isotopic ratio. It is a clear evidence that fractional crystallization cannot explain their major element (e.g. K, Na, Mg) geochemical evolution.

However, we tested whether the multiple fractional crystallization trends with different starting components, may explain the trace element variations related to fractional crystallization (see Supplementary Table S3 and Fig. S5 for details of the fractional crystallization modelling). For the initial fractional crystallization path, we follow a fractional crystallization model from the lavas having the least diverse zoning types in clinopyroxene (pillow lava; M-128). Accordingly, the REE concentrations of analcime and analcime-bearing lavas cannot be explained by a significant mineral fractionation of a melt with a composition equivalent to that of pillow lavas (Fig. S5a). Accordingly, higher Na_2O contents and a positive correlation with LOI in these lavas can be explained by secondary processes. Alternatively, it is possible that the occurrence of alkali sodic feldspar in the more evolved lavas led to elevated concentrations of Ba and Sr and a positive correlation between both elements and Na_2O. However, high Na_2O, Sr and Ba contents are also

observed in the more primitive tephrite dykes having low LOI. This pattern suggests that such elemental concentrations may represent an intrinsic characteristic of parental melts rather than the effect of mineral phases.

For the second fractional crystallization path, we modelled trace element concentrations resulting from the fractional crystallization of a primary lamprophyre (e.g. minette; Buhlmann *et al.*, 2000; Fig. S5b). Accordingly, none of the element concentrations of lamprophyres—having the highest modal content of colourless or grass green macrocrysts—can be explained by the crystal fractionation model. Surprisingly, tephrite dykes having a similar range of MgO as lamprophyres also show a limited variability for major elements, even where their trace element concentrations plot near to those of pillow lavas. Thus, these results clearly show that fractional crystallization cannot fully explain the variations in chemical elements, particularly within lamprophyres and tephrite dykes.

Macrocrysts

Antecrysts versus phenocrysts

As mentioned above, the most distinctive characteristic of the samples having an unusual whole-rock composition is the variation of the modal content of the mega/microcrysts of clinopyroxene (e.g. lamprophyre and tephrite dykes). To test the equilibrium or disequilibrium states of zoned macrocrysts and host lavas, we calculate the Mg# of a hypothetical melt that is in equilibrium with macrocrysts (the calculation relies on $Kd\ ^{mineral-melt}_{Fe-Mg}$; 0.26 ± 0.05 taken from Akinin *et al.,* 2005). We find that the colourless zone in Type-I with high Mg# plots above the calculated equilibrium melt curve (Fig. 11), whereas the grass green clinopyroxene (Type-III) plot below the curve. This pattern indicates the lack of a long-term equilibrium with the host. Interestingly, pale green Type-

IVa macrocrysts in pillow lavas and the rim of Type-I macrocrysts in tephrites plot on or just slightly below the curve. We cannot consider these as phenocrysts on the basis of the position of the colourless and green clinopyroxenes, relative to the curve, and the petrographic observations, i.e. the occurrence of a dissolution surface between the corroded cores and the overgrowth rims combined with the mineral elemental maps. The best term to describe these mega- and macrocrysts is *antecryst*, i.e. large crystals that are not in chemical equilibrium with the surrounding magma but that have crystallized from a more primitive melt of either the same source or completely different melts (Davidson *et al.*, 2007; Larrea *et al.*, 2012). Generally, macrocrysts that are cogenetic with host lavas are classified as *phenocrysts*.

Macrocryst accumulation

Mafic crystal cargo clearly and greatly affects whole-rock composition; bulk samples integrate the crystals and the melt transporting these crystals (e.g. Ubide *et al.*, 2014). In tests of the effect of crystal accumulation, microlithic rocks can be considered as representative of true liquids. The lowest porphyricity index belongs to the pillow lavas, which, notably, contain no antecrysts. Thus, pillow lavas could represent a composition that is not affected by the accumulation process. In Harker diagrams (Fig. S4), the diversity observed in the investigated antecryst-bearing lavas becomes apparent when recycled clinopyroxenes, or in some cases olivine+clinopyroxene, are added to the initial whole-rock composition. The marked accumulation of colourless and grass green core antecrysts (Type-I and III) with higher and lower Mg#, respectively alter the whole-rock composition. This pattern is consistent with Fig. 11, which clearly illustrates how whole-rock composition is affected by accumulation—colourless antecrysts plot immediately above the curve for lavas that are characterized by the highest Mg# and modal content of these antecrysts.

Potential origin of antecrysts

Geobarometry to estimate crystallization depth

To explore the links between crystallization depth and clinopyroxene composition, we apply Equation 32b from Putirka (2008), as adapted from Nimis (1995). This equation is appropriate for mineral crystallized in water-rich melts. In our study, melt composition is obtained from whole-rock analyses of the lavas, the water content assumption is similar to the given range for high-pressure alkaline melts (e.g. up to 6 wt %; Sato, 1997). Thus, we selected minette (M-112) and pillow lava (M-128) as being representative of liquid composition in equilibrium with colourless and grass green core antecrysts, respectively, because i) these two samples have highest modal content of Type-I and IVa, respectively; ii) they contain only a single type of zoned clinopyroxene; and iii) the melt in equilibrium with Type- IVa phenocrysts in pillow lavas is similar to the melt in equilibrium with Type-III antecrysts in lamprophyres.

The estimated crystallization pressures of the different types of zoned clinopyroxenes are provided in the Supplementary Table S4. Colourless antecrysts and cumulates (Type-I) from volcanic breccias, kersantite lamprophyres, tephrite dykes and clinopyroxenite cumulates produce similar pressure estimates of 1.1–1.5 GPa (Fig. 12). Colourless antecrysts from minette lamprophyre provide slightly lower values (0.8–1 GPa). In contrast, colourless antecrysts (Type-II) from tephrites yield higher crystallization pressures of ~2 GPa. Reverse-zoned grass green core antecrysts (Type-III) have an estimated pressure of ~1 GPa, a value similar to the values for the clinopyroxenes in pillow lavas, mica-bearing cumulates and along the rim of the clinopyroxenite cumulates. From these values, the estimated crystallization depth within the uppermost mantle corresponds to ~60 km. We obtained similar pressure estimates (~2 GPa) for the clinopyroxene

crystallization of the lamprophyres and the associated cumulates from the surrounding regions (e.g. Turkey, Semiz *et al*. 2012; Prelević *et al*., 2015).

Grass green core antecrysts

The marked zoning pattern in antecrysts highlights their magmatic evolution. Regardless of crystallization depth, the compositional gap observed between the colourless and grass green core antecrysts indicates that the antecrystals may have originated from different melts derived from a single or multiple sources (e.g. Tappe, 2004; Orejana *et al.*, 2007; Larrea *et al.*, 2012; Grützner *et al.*, 2013).

In regard to the hypothesis of a single melt, we must assume that the initial host melt (high in Mg#) was in equilibrium with the colourless antecrysts; it evolved eventually by fractional crystallization into a lower Mg# melt that was in equilibrium with the grass green core antecrysts. Such an assumption, however, is at odds with some observations: (i) the lack of crystals of intermediate composition, and (ii) both types of colourless and grass green core antecrysts have resorption surfaces where they occur together within the same sample. Therefore, none of the antecrysts would be in equilibrium with the host melt. On the other hand, the increase in f_{H2O} and/or f_{O2} reduces silica activity and leads to the incorporation of Fe^{+3}, Al and Ti into the clinopyroxene structure. A change in redox conditions, because of the crystallization of Fe–Ti oxides (e.g. magnetite), may lead to a lowering of the Fe content of the melt. This process could explain the higher Fe^{+3}, Al and Ti contents of the grass green antecrysts (Type-III); however, petrography does not provide any evidence for the crystallization of Fe-oxides and grass green core antecrysts. On the contrary, they are associated preferentially with colourless antecrysts (Type-I). The experimental results from Mollo *et al*. (2010) indicate that the Na and Al contents of clinopyroxene

increase, whereas those of Mg and Ca (and Fe^{+2}/Fe^{+3}) decrease with an increased cooling rate. Furthermore, a change in the mineral cargo of crystals of constant isotopic ratios will not affect the whole-rock isotopic composition (e.g. Davidson *et al.*, 2007). Combining evidence from mineral and whole-rock compositions, including isotopes, and from the distribution of clinopyroxene in the various lithologies allows us to discard fractional crystallization due to cooling as the unique parameter governing the evolution of our samples.

Colourless antecrysts

Colourless microcrysts or macrocrysts are common in alkaline ultrapotassic–potassic lavas; they are interpreted as relatively high-pressure clinopyroxenes that crystallized within the upper mantle (e.g. Semiz *et al.*, 2012; Prelević *et al.*, 2015; Jankovics *et al.*, 2016). Petrography and mineral chemistry show no evidence for a strongly evolved melt (e.g. the absence of quartz or feldspar phenocrysts) for rocks having a high modal abundance of colourless antecrysts. In contrast, resorption surfaces of olivine and colourless antecrysts are robust evidence for the involvement of a relatively high Mg# melt. As observed in Fig. 13, the major element composition of colourless antecrysts ties well with the composition of colourless clinopyroxene from alkaline rocks. Similar results are obtained for grass green core antecrysts. Generally, the low Al and Ti contents of colourless antecrysts are consistent with the main characteristics of extremely potassium-rich melts (Rock 1991).

By comparing the composition of these clinopyroxenes with that derived from experimental studies, we can better constrain the characteristics of the involved melts. As expected, we observe that the composition of colourless antecrysts is broadly similar to that of clinopyroxene in equilibrium with melts at high pressure (2–3 GPa; Fig. 13a). It is important to highlight that this

composition requires a crystal to be in equilibrium with a melt that contains at least 2 wt % H_2O and 4–6 wt % K_2O (see Lloyd *et al*., 1985). Importantly, such observations are consistent with the mineral compositions estimated via MELT simulations that depend on the hypothetical parental melt having a kamafugitic composition at 1.5 GPa (from Prelević *et al*., 2015; Fig. 13b). We obtain a similar result by evaluating the trace element content of antecrysts. The LREE content of colourless antecrysts is markedly lower than that of grass green core antecrysts; the content is also more consistent with that of clinopyroxenes in kimberlites (Kamenetsky *et al.,* 2009). More generally, these geochemical findings are consistent with previous studies that demonstrate that exotic melts (i.e. kamafugite, lamproite and lamprophyre) are the parental magmas of some ultramafic clinopyroxene-rich cumulates (e.g. Semiz *et al*., 2012; Prelević *et al*., 2015). Hence, as mentioned above, it is more likely that this antecryst diversity relates to various parental melt compositions.

Linkages between antecrysts and alkaline magmatism within the Turkish-Iranian plateau

Origin of antecrysts and their relationship to alkaline lavas from the Turkish-Iranian plateau

The studied samples, which are similar to the potassic lavas collected from across the plateau, plot between the ultrapotassic and sodic lava fields. As presented above, there is a clear link between the modal content of antecrysts and the whole-rock alkali content. We can therefore propose to extend this correlation beyond the antecrysts of this study to other potassic and sodic alkaline lavas from the Turkish-Iranian plateau.

In the clinopyroxene-melt equilibrium diagram, the closest Mg# values of melts in equilibrium with grass green core antecrysts (Type-III) are those from pillow lavas (Type-IVa). In Fig. 14a, we plot the trace element concentration of lamprophyre dykes with the high modal abundance of

colourless and grass green core antecrysts (M-112 and M-113, respectively). Lamprophyres having a higher abundance of grass green core antecrysts show higher trace element contents. Interestingly, they have trace element patterns similar to those of pillow lavas. This observation is fully consistent with the high incompatible trace element content of both types of clinopyroxene in those lavas. The similarity of the mineral composition of Type-III and IVa and the similar influence they have on the whole-rock geochemistry of their host lavas lead us to consider them as crystals that are in equilibrium with similar melts. If we combine these observations with our above-mentioned results in the "macrocryst accumulation" section, we can state that they are representative of a relatively evolved melt that is low in Mg and high in Al and Na with a high $^{143}Nd/^{144}Nd$.

We can then determine whether the mixing model is consistent with REE patterns from the melt in equilibrium with the colourless and grass green antecrysts and from a series of representative ultrapotassic and sodic melts. The melt in equilibrium with colourless antecrysts (Type-II) may represent the most primitive component by having (i) high Cr and Mg and (ii) a trace element content similar to that of the exotic melts. The mixing of the ultrapotassic and sodic melts can explain the trace element content of the lamprophyres. Nonetheless, there are samples having a high modal content, such as the colourless antecrysts (Type-I), and a lower REE content, as for the Type-II antecrysts. Apart from mixing, the trace element content of the melt in equilibrium with colourless Type-I antecrysts could have been modified by crustal contamination processes, as evidenced by their (i) slightly higher Sr ratios and (ii) slightly lower trace element content relative to those of the primitive minettes (Fig. 14a). Type-I antecrysts also crystallized at a shallower depth than the Type-II antecrysts. At depths that correspond to the ponding of the melt within the crust—that offer a higher possibility for crustal contamination to occur, particularly due

to the hotter primary magma—the greatest amount of crust assimilation may occur (see Supplementary Material B). Melts in equilibrium with grass green core antecrysts or pillow lavas are explained by fractional crystallization from sodic alkaline melt from the Turkish-Iranian plateau; this crystallization leads to the enrichment of incompatible trace elements from a more primitive melt (e.g. Fig. 14a).

To assess in greater detail the characteristics of the source, we produce a mixing model between the average composition of global OIB and the primitive minette derived from EM-I. We calculated four mixing trends (Fig. 14b): (1) a mixing model between two endmembers of a heterogeneous source (depleted mantle vs pelagic sediments) and sodic alkaline lavas (OIB-like) from the Turkish-Iranian plateau, (2) a mixing model between the two endmembers of sodic and ultrapotassic lavas from NW Iran, (3) a mixing model of a depleted sodic melt endmember (Allegre *et al*., 1979) and a primitive minette (Buhlmann *et al*., 2000) and (4) a mixing model using similar composition to (1), although GLOSS having lower $^{87}Sr/^{86}Sr$. Pillow lavas plot close to the sodic lavas along the mixing lines. Moreover, lamprophyres containing a high modal abundance of grass green core antecrysts plot close to the sodic alkaline lavas (OIB-like). The greater the ultrapotassic and/or lamproite melt involvement in the mixing, the greater the abundance of colourless antecrysts.

The location of the endmember corresponding to the melt derived from a hybrid source depends on the initial isotopic composition of the sediment component (e.g. GLOSS, $^{87}Sr/^{86}Sr$: 0.71730; Plank & Langmuir, 1998). The isotopic composition of seawater varies over geologic time, a feature that may influence the Sr isotope ratio of subducted materials (Veizer, 1989). Accordingly, high $^{87}Sr/^{86}Sr$ values are interpreted traditionally in terms of modern pelagic sediments or continental crustal rocks (e.g. Plank & Langmuir, 1998), whereas lower values can represent

sediments derived from a stagnant slab, the "second continent material" from the mantle transition zone (e.g. Rapp *et al.*, 2008) or both; this process then leads to heterogeneities within the upper mantle (e.g. Fukao *et al*., 2001). Such components may be those involved in the multistage model proposed by Förster *et al.* (2020) to explain the origin of extremely K_2O-rich mantle melts. Recently, Soltanmohammadi *et al.* (2018) demonstrated that strong anomalies observed in tomography seismic images from below the Turkish-Iranian plateau are linked to mantle melts and components through "compaction pockets" originating from the mantle transition zone. Hence, it is not surprising that in the geochemical modelling of a heterogeneous source, the $^{87}Sr/^{86}Sr$ ratio of sediments does not fit that of modern pelagic sediments but rather that of ancient sediments. Interestingly, our samples better fit with the line 4 of mixing for melts derived from heterogeneous sources, which are relatively low in $^{87}Sr/^{86}Sr$.

Implications of melts being derived from compaction pockets and the origin of antecrysts

Alkaline melts cannot be derived from a "normal" mantle, regardless of the complexity of igneous evolution invoked. Additional sources are required to explain their geochemical characteristics (Hirschmann *et al.*, 2003; Rapp *et al.*, 2008; Brey *et al.*, 2011;). One category of scenarios invokes processes specific to mantle wedge environments, such as the occurrence of a hydrated mantle located on top of a flat slab or the rise of a hot mantle flow during slab break-off, rollback or slab tearing (Davies & von Blanckenburg, 1995; Rosenbaum *et al*., 2008). After such an event, during the syn- to post-collisional processes, crustal thickening leads to delamination and/or decompression melting of the metasomatized subcontinental lithosphere or the emplacement of a hot mantle at the base of the crust (François *et al.*, 2014). According to these classical geodynamic mechanisms, a hot mantle is needed to explain the occurrence of silica-undersaturated alkaline melts. Furthermore, we have shown that the petrological and geochemical characteristics of the

Salavat Range lavas require the involvement of both ultrapotassic and sodic alkaline melts similar to those from the entire Turkish-Iranian plateau. It is important to note that none of the above-mentioned mantle sources (subducted slab or asthenospheric mantle at a shallow depth) can explain the silica-undersaturated ultrapotassic melts. Moreover, if the temperature is high at a shallow depth (for example ~1300°C at 60 km), the melting of the convecting mantle will erase any signature of a low-degree melting-derived melt and lead to the formation of high-degree melting-derived melts (Green, 2015; Pilet, 2015).

The presence of two types of antecrysts (±cumulates) in the same sample indicates that ultrapotassic and sodic melts travel via the same melt trajectories (i.e. dykes). The production of dykes in a mantle mush requires two related conditions: (i) a strong obstruction to the upward percolation of melt that results in the melt accumulating below the blocking horizon (Rabinowicz *et al*., 2002; Grégoire *et al.*, 2006) and (ii) an excessive pressure at the top of the zone of melt accumulation that exceeds the yield strength of the partially molten rock (Spera, 1987). This process is linked directly to the development of compaction waves (Grégoire *et al.*, 2006).

The main characteristics of the Turkish-Iranian plateau are (i) the absence of a mantle plume and long-lasting subduction (e.g. Kaviani *et al*., 2018), (ii) a great diversity of alkaline magmatism and (iii) a large set of scattered low-velocity bodies down to the mantle transition zone (Soltanmohammadi *et al.*, 2018). Recently, Soltanmohammadi *et al.* (2018) proposed a model that highlights the importance of the mantle transition zone where a large volume of recycled materials accumulated during the various phases of a previous subduction cycle. These lithospheric fragments, which ponded in the transition zone, may continuously cool the upper mantle below the Turkish-Iranian plateau by 100–200°C. As such, Soltanmohammadi *et al.* (2018) adapted the dimensionless model proposed by Grégoire *et al.* (2006) to introduce parameters adapted to the

case of the Turkish-Iranian plateau (e.g. a viscosity of 10^{20} Pa·s for a wet-cold mantle (100°C below the mantle adiabat). They observed low-velocity seismic anomalies under the entire plateau and interpreted these anomalies as ~100-km-wide compaction pockets; these pockets result from the obstruction induced by mineral crystallization in compaction waves. Soltanmohammadi *et al.* (2018) suggested that hydrated and carbonated mineral phases are likely the main cause of multistage drops in permeability (e.g. richterite is stable down to 6.5 GPa at 1350°C; Konzett et al., 1997). The modelling reveals that during the ascent of the compaction pocket, the effective stress at its top is sufficiently high to induce the formation of melt-filled dykes at the approximate depths of 240 km (8 GPa), 165 km (5.5 GPa) and 135 km (4.5 GPa). The three defined alkaline lavas observed within the Turkish-Iranian plateau (ultrapotassic, sodic-(I) and -(II), see Soltanmohammadi *et al*., 2018) are tentatively linked to these three successive melt-extraction events. The main characteristic of these alkaline melts is that they flowed within dykes located near the borders of the compaction pockets and crossed the entire lithosphere without any significant interaction with their host peridotite. There is a combination of physicochemical processes that may lead the extracted melts transported by dykes to pond at different depths; for example, cumulative xenoliths result from the reaction at the interface between a differentiating basic melt and the carbonate host rock (at crustal level) before eruption (e.g. Di Rocco *et al.,* 2012). The main geochemical characteristics of the antecrysts in the investigated lavas demonstrate, however, that they were not affected by crustal contamination (neither carbonate nor granitoid, see Supplementary Material B). Simply put, ponding of the melt may occur at interfaces of contrasting density, such as the density stratification induced by the garnet–spinel transition (~2 GPa) and the lithological contrast at the crust-mantle interface (~1 GPa) (e.g. Fig. 15). According to the compaction model, the characteristic time interval separating the development of Stage I and Stage III dyke swarms is ca. 0.3 Ma. To prevent the complete crystallization of Stage I melts, the

temperature in the ponding horizon must be ~1000°C (e.g. Eggler, 1989). In NW Iran, the crust is 40- to 55-km thick, the Moho temperature varies between 700 and 800°C and the lithosphere is less than 120-km thick; this last condition implies that the temperature gradient across the entire lithosphere exceeds $10°C \cdot km^{-1}$ (Motavalli-Anbaran *et al.,* 2016). Therefore, the ponding horizon may be located at a depth of ~70 km, a depth close to that of the spinel–garnet transition. We consider that colourless antecrysts and cumulates are cogenetic and crystallized at relatively high pressures from extreme potassium-rich melts derived from the first stage of compaction pocket formation. (Fig. 15). Assuming that the overlying lithosphere was not tectonically stressed when the Stage I melts were formed, the density jump at the spinel–garnet interface may have lead by itself to a vertical stretching of the lithosphere at that depth ($\vec{\sigma}_3$ is vertically oriented) and thus the ponding of the melts at later stages (e.g. Rigo *et al.*, 2015).

Finally, when the compaction pockets collide with the overlying lithosphere ca. 0.3 Ma later, the vertical uplift induced by these compaction pockets leads to the rotation of $\vec{\sigma}_3$ to the horizontal. This would explain how dykes channelize the later stage (e.g. sodic) melts, which are mixed almost instantaneously with partly crystallized patches of Stage I melts—as well as being brought closer to the surface—and pond 0.3 My earlier at about 70 km depth. Later, the interaction between the newly arriving melts (sodic) and the resident crystal-rich mushes may have rapidly disaggregated and mobilized the near-solidus crystals formed from the earlier ponded melts. The resulting melt fraction at the different stages (crust–lithosphere interface) led to the formation of the various mineral assemblages. This scenario could account for the occurrence of phlogopite-bearing clinopyroxenite or monzogabbro cumulative xenoliths observed in our study area. The compositional zoning of their constituent minerals, their host lavas and their clinopyroxene composition are transient between colourless and grass green core antecrysts. Thus, we consider

them as cumulates formed after the arrival of sodic melt through ultrapotassic mush. Finally, in the specific case of a local ponding melt at the middle- to lower-crust level, contamination of the mantle-derived melts by continental crust can explain the crustal contamination signature of lamprophyre features. On the other hand, magma chamber dynamics are generally cited to explain oscillatory and sector zonings observed in some crystals (e.g. convective self-mixing; Couch *et al.* (2001); Streck, (2008)) or their growth with variable chemistries along different crystallographic orientations (e.g. Ubide *et al*., 2019), even when melt composition, pressure, temperature and water content remain constant. We propose that such types of shallow crustal level magmatic processes are likely responsible for forming pale green phenocrysts (Type-IVb) with oscillatory and sector zonings (e.g. Ubide & Kamber, 2018; Ubide *et al*., 2019).

CONCLUSIONS

This study is the first step toward enhancing an understanding of the impact of variable macrocryst content on the whole-rock composition of alkaline magmatic rocks from NW Iran. We demonstrate that the alkaline potassic affinity of the investigated lithologies reflects the abundance of clinopyroxene macrocryst cargo. Four types of clinopyroxene antecrysts and phenocrysts are defined: colourless (Type-I and -II) and grass green (Type-III) concentric zoned antecrysts as well as grass green and pale green oscillatory-sectored zoned phenocrysts (Type-IV). In regard to the clinopyroxene antecryst cargo, our classification relates to a very large difference in melt composition at equilibrium for the colourless and grass green antecrysts. There is an exotic (i.e. ultrapotassic-low silica) melt characterized by relatively low REE concentrations and $^{143}Nd/^{144}Nd$ values that are in equilibrium with the colourless antecrysts, whereas a sodic melt characterized by higher REE concentrations and higher $^{143}Nd/^{144}Nd$ values appears to be in equilibrium with the grass green antecrysts.

The petrological and geochemical data presented here agrees well with the compaction pocket model proposed by Soltanmohammadi *et al.* (2018), a model that relates the potassic affinity of magmas from NW Iran to multistage alkaline ultrapotassic and sodic melt-extraction processes from ascending compaction pockets. It is therefore critical to interpret the characteristics of potassic rocks within a framework of multiple sources. Further studies focusing on shallow crustal processes will allow us to refine this model with more emphasis on the origin and meaning of the phenocrysts with sectored and oscillatory zoning patterns (e.g. Ubide & Kamber, 2018; Ubide *et al*., 2019).

ACKNOWLEDGEMENTS

The research has been financially supported by CNRS, (France). We thank A. Cousin, the graphic designer of the GET for drawing the final figures. We also thank P. de Parseval and J. Chmeleff and A. Marquet for their assistance with electron microprobe and laser ICP-MS analyses, respectively. We appreciated the constructive reviews made by T. Ubide and two anonymous reviewer that significantly improved the paper. We finally thank M. Humphreys' editorial assistance that also greatly improved the manuscript.

DATA AVAILABILITY

The data underlying this article are available in the article and in its online supplementary materials [link].

FIGURE CAPTIONS

Fig. 1 (a) Simplified geological map covering Cenozoic–Quaternary magmatism from East Anatolia to NW Iran (modified from Haghipour *et al.* (2009)). (b) Geological map showing the distribution of Cenozoic magmatism in the Salavat Range (modified after Babakhani *et al.*, 1990). (c) Cross-section (A–A') from the north to the centre of the Salavat Range. Key features: AMZ: Azerbaijan magmatic zone; UL Urmieh Lake; VL, Van Lake; SV, Sevan Lake; Quaternary volcanoes (triangles); SH, Sahand; SB, Sabalan.

Fig. 2 Field photographs showing outcrops of (a) lamprophyre dykes that cross-cut the volcanic breccia and pillow lavas. (b) Pillow structures vary in shape and size. (c) Tephrite dykes contain horizontal columnar joint structures. (d) Tephrite dykes cross-cut both lamprophyre and volcanic breccia. (e) Ultramafic and (f) mafic cumulative xenoliths are hosted by lamprophyres. Analcime-bearing lavas display (g) columnar joint structures covered by Oligocene–Miocene sedimentary rocks (h).

Fig. 3 Histograms comparing (a) the modal abundance of mineral assemblages, alkali elements and LOI contents and (b) various zoned clinopyroxenes of igneous rocks collected from the Salavat Range. The symbol * indicates that sample has been considered to be affected by alteration.

Fig. 4 (a) Chemical classification (Mg–Ca–Fe mol%) diagrams for colourless and green-zoned clinopyroxenes from the studied lavas (after Morimoto, 1988); compositional fields of lamproites and lamprophyres after Rock (1991). (b–k) Variation in major elements from core to rim (C–R line in c) in grass green (Type-III) zoned clinopyroxenes from kersantite.

Fig. 5 Variation in major elements from core to rim (C–R line in b) in colourless (Type-II) clinopyroxene from tephrite dykes (a–f), as well in (g–l) colourless (Type-I) zoned clinopyroxenes from clinopyroxenite cumulates and (m–r) kersantite.

Fig. 6 Diagrams presenting the average concentration of trace elements in different zoned clinopyroxenes normalized to chondrite (Sun & McDonough, 1989). REE concentrations of clinopyroxenes from kimberlite are from Kamenetsky *et al.* (2009).

Fig. 7 Variation in major elements from core to rim (C–R line in b) in oscillatory-sectored zoned clinopyroxenes (Type-IVb) from tephrite.

Fig. 8 (a–d) Variation in major elements among the types of zoned clinopyroxenes. Fields marked by numbers are representative compositions of clinopyroxenes from worldwide alkaline magmatism: 1) colourless clinopyroxene from Vulsini, Italy (Barton *et al.*, 1982); (2) cumulative xenoliths from Spain (Orejana & Villaseca, 2008) and Turkey (Semiz *et al.*, 2012); colourless clinopyroxenes from Leucite Hill (Barton & van Bergen, 1981); (3) cumulative xenoliths, Turkey (Semiz *et al.*, 2012), lamprophyres, Iran (Aghazadeh *et al.*, 2015); (4) Mg-rich clinopyroxenes from lamprophyres, Spain (A-type in Ubide *et al*., 2014); (5) colourless clinopyroxenes, Kazakhstan (Zhu & Ogasawara, 2004); (6) green clinopyroxenes, Kazakhstan (Zhu & Ogasawara, 2004); (7) green clinopyroxenes from Leucite Hill (Barton & van Bergen, 1981).

Fig. 9 (a) Total alkali vs silica diagram (Le Maître, 2002); (b) K_2O vs Na_2O diagram for the classification of the studied rocks. The data for alkaline lavas from the Turkish-Iranian plateau are from the literature (see references in Soltanmohammadi *et al*., 2018) Patterns of (c) whole-rock trace elements and (d) REE normalized to the primitive mantle and chondrite values (Sun & McDonough, 1989). The values in figures c and d are mean compositions for different category

of rock samples. Other reference sources are oceanic island basalt (OIB; Sun & McDonough 1989), primitive minette (Buhlmann *et al.*, 2000) and lamproites derived from the mantle transition zone (Murphy *et al.*, 2002).

Fig. 10 Whole-rock Sr–Nd isotope ratios vs whole rock major elements (wt %) (a–d) and modal abundance of different types of clinopyroxene (e–f) for the studied lavas. The red arrows in figures a–d are derived from figures e–f and reflect the increasing mode of the various types of zoned clinopyroxenes in different rock types; symbols are as in Fig. 9a. The black arrow estimates the change of composition related to mantle sources (OIB, EM-I and -II), continental crust (CC) and fractional crystallization (FC). The alkaline lavas from the Turkish-Iranian plateau are plotted for comparison purposes. (e and f) The grey fields show the correlation between modal abundance of crystal types- III and -IVa and the whole-rock Sr and Nd isotopic compositions of different kind of rock types presented in figures a-d.

Fig. 11 Mg# in clinopyroxene (cpx) vs Mg# in a whole-rock diagram. The black curve represents the mineral-melt equilibrium according to the Fe–Mg exchange (after Rhodes *et al.*, 1979) using the distribution coefficient ($Kd_{Fe–Mg} = 0.26 \pm 0.05$) of Aknin *et al.* (2005).

Fig. 12 Pressure of crystallization estimated for different types of zoned clinopyroxenes from the studied lavas and cumulative xenoliths. For comparison, the pressure of mineral crystallization for cumulative xenoliths hosted in similar alkaline lavas are presented; these latter samples are from Spain (Orejana & Villaseca, 2008) and Turkey (Prelević *et al.*, 2015; Semiz *et al.*, 2012).

Fig. 13 CaO vs (a) Al_2O_3 and (b) MgO contents (wt %) in colourless (Types-I and -II), grass green (Type-III) zoned clinopyroxenes from cumulative xenoliths and lavas from this study; symbols are as in Fig. 8. Worldwide green clinopyroxenes are from Spain (Orejana *et al.*, 2007;

low MgO zoned clinopyroxenes from Ubide *et al.*, 2014); Leucite Hill, Wyoming (Barton & van Bergen, 1981) and Kazakhstan (Zhu & Ogasawara, 2004). Colourless clinopyroxenes are also from the above-mentioned references with the addition of cumulates from Turkey (Semiz *et al.*, 2012) and high-MgO zoned clinopyroxene from Ubide *et al.* (2014). Green clinopyroxene hosted in non-orogenic alkaline rocks are from Massif Central (Pilet *et al.*, 2002) and Eifel (Duda & Schmincke, 1985). The shaded field in (a) is clinopyroxene content from different experimental studies, modified after Semiz *et al*. (2012). In (b), the high-pressure cumulative xenolith from Turkey and MELTS calculations at various crystallization pressures for exotic melts (e.g. kamafugite and lamproites) at fixed water contents of 1 and 2 wt % are from Prelević *et al*., 2015.

Fig. 14 (a) Diagram presenting REE concentrations of ultrapotassic and sodic alkaline lavas from the plateau and REE concentrations of theoretical melts in equilibrium with colourless (Type-I and-II), grass green (Type-III) and pale green (Type-IVa) clinopyroxenes (symbols as in Fig. 6). Melt calculations are based on $Kd_{\text{mineral-melt}}$, as proposed by Keshav *et al.* (2005) for exotic melts in equilibrium with colourless clinopyroxene, whereas green clinopyroxene partition coefficients are from Ubide *et al.* (2014). In this diagram, results are compared with whole-rock samples having the highest modes of colourless clinopyroxene and green core clinopyroxene, respectively. Dashed lines represent the mixing of averaged lamproites and OIB-like melts from the Turkish-Iranian plateau. The continental crust average is from Hofmann (1988). References for OIB, primitive minette and lamproites are the same as in Fig. 9. (b) A $^{143}Nd/^{144}Nd$ vs $^{87}Sr/^{86}Sr$ diagram illustrating the 4 mixing lines between the different endmembers; see text for detail of endmembers used to calculated mixing lines. Symbols are as in Fig. 9a.

Fig. 15. Simplified schematic diagram showing the three stages of the ascent of compaction pockets through the upper mantle and the associated melt compositions, as proposed by

Soltanmohammadi *et al*. (2018). According to the mineral and whole-rock chemistry of the lavas, the geochemical characteristics of the melts extracted from Stage 1 (ultrapotassic) and Stage 3 (sodic) explain the formation of the various cumulates and both types of antecrysts, colourless and grass green antecrysts, hosted in the studied lavas.

REFERENCES

Aghazadeh, M., Prelević, D., Badrzadeh, Z., Braschi, E., van den Bogaard, P. & Conticelli, S. (2015). Geochemistry, Sr-Nd-Pb isotopes and geochronology of amphibole-and mica-bearing lamprophyres in northwestern Iran: Implications for mantle wedge heterogeneity in a palaeo-subduction zone. *Lithos* **216**, 352-369.

Akinin, V. V., Sobolev, A. V., Ntaflos, T. & Richter, W. (2005). Clinopyroxene megacrysts from Enmelen melanephelinitic volcanoes (Chukchi Peninsula, Russia): application to composition and evolution of mantle melts. *Contributions to Mineralogy and Petrology* **150**, 85-101.

Alberti, A. A., Comin-Chiaramonti, P., Di Battistini, G., Nicoletti, M., Petrucciani, C. & Sinigoi, S. (1976). Geochronology of the Eastern Azerbaijan volcanic plateau (North-west Iran). *Rendiconti della Societa Italiana di Mineralogia e Petrologia***32**, 579-589.

Allegre, C. J., Othman, D. B., Polve, M., & Richard, P. (1979). The Nd- Sr isotopic correlation in mantle materials and geodynamic consequences. *Physics of the Earth and Planetary Interiors* **19**, 293-306.

Babakhani, A. R., Lesquyer, J. L. & Rico, R. (1990). *Geological map of Ahar quadrangle (scale 1: 250,000).* Geological Survey of Iran.

Barton, M., & van Bergen, M. J. (1981). Green clinopyroxenes and associated phases in a potassium-rich lava from the Leucite Hills, Wyoming. *Contributions to Mineralogy and Petrology* **77**, 101-114.

Barton, M., Varekamp, J. C. & Van Bergen, M. J. (1982). Complex zoning of clinopyroxenes in the lavas of Vulsini, Latium, Italy: evidence for magma mixing. *Journal of Volcanology and Geothermal Research* **14**, 361-388.

Becker, M. & Le Roex, A. P. (2006). Geochemistry of South African on- and off-craton, Group I and Group II kimberlites: petrogenesis and source region evolution. *Journal of Petrology* **47**, 673–703.

Brey, G. P., Bulatov, V. K. & Girnis, A. V. (2011). Melting of K-rich carbonated peridotite at 6-10 GPa and the stability of K-phases in the upper mantle. *Chemical Geology* **281**, 333-342.

Buhlmann, A. L., Cavell, P., Burwash, R. A., Creaser, R. A., & Luth, R. W. (2000). Minette bodies and cognate mica-clinopyroxenite xenoliths from the Milk River area, southern Alberta:

records of a complex history of the northernmost part of the Archean Wyoming craton. *Canadian Journal of Earth Sciences* **37**, 1629-1650.

Castro, A., Aghazadeh,M., Badrzadeh, Z. & Chichorro, M. (2013). Late Eocene-Oligocene post-collisional monzonitic intrusions from the Alborz magmatic belt, NW Iran. An example of monzonite magma generation from a metasomatized mantle source. *Lithos* **180-181**, 109-127.

Comin-Chiaramonti, P., Meriani, S., Mosca, R. & Sinigoi, S. (1979). On the occurrence of analcime in the northeastern Azerbaijan volcanics (northwestern Iran). *Lithos* **12**, 187-198.

Condamine, P. & Médard, E. (2014). Experimental melting of phlogopite-bearing mantle at 1 GPa: Implications for potassic magmatism. *Earth and Planetary Science Letters* **397**, 80-92.

Condamine, P., Médard, E. & Devidal, J.-L. (2016). Experimental melting of phlogopite-peridotite in the garnet stability field. *Contributions to Mineralogy and Petrology* **171**, p.95.

Conticelli, S. (1998). The effect of crustal contamination on ultrapotassic magmas with lamproitic affinity: mineralogical, geochemical and isotope data from the Torre Alfina lavas and xenoliths, Central Italy. *Chemical Geology* **149**, 51-81.

Couch, S., Sparks, R. S. J. & Carroll, M. R. (2001). Mineral disequilibrium in lavas explained by convective self-mixing in open magma chambers. *Nature* **411**, 1037-1039.

Davidson, J. P., Morgan, D. J., Charlier, B. L. A., Harlou, R. & Hora, J. M. (2007). Microsampling and isotopic analysis of igneous rocks: implications for the study of magmatic systems. *Annual Review of Earth Planetary Science **35***, 273-311.

Davies, J. H., & von Blanckenburg, F. (1995). Slab breakoff: a model of lithosphere detachment and its test in the magmatism and deformation of collisional orogens. *Earth and Planetary Science Letters* **129**, 85-102.

Di Rocco, T., Freda, C., Gaeta, M., Mollo, S. & Dallai, L. (2012). Magma chambers emplaced in carbonate substrate: petrogenesis of skarn and cumulate rocks and implications for CO_2 degassing in volcanic areas. *Journal of Petrology* **53**, 2307-2332.

Duda, A. & Schmincke, H. U. (1985). Polybaric differentiation of alkali basaltic magmas: evidence from green-core clinopyroxenes (Eifel, FRG). *Contributions to Mineralogy and Petrology* **91**, 340-353.

Eggler, D. H. (1989). Kimberlites: How do they form? In Kimberlites and Related Rocks (ed. J. Ross) *Blackwell* **1**, 489-504.

Foley, S. (1992). Vein-plus-wall-rock melting mechanisms in the lithosphere and the origin of potassic alkaline magmas. *Lithos* **28**, 435-453.

Förster, M. W., Buhre, S., Xu, B., Prelević, D., Mertz-Kraus, R., & Foley, S. F. (2020). Two-stage origin of K-enrichment in ultrapotassic magmatism simulated by melting of experimentally metasomatized mantle. *Minerals* **10**, 41.

Förster, M. W., Prelević, D., Schmück, H. R., Buhre, S., Veter, M., Mertz-Kraus, R., & Jacob, D. E. (2016). Melting and dynamic metasomatism of mixed harzburgite+ glimmerite mantle source: Implications for the genesis of orogenic potassic magmas. *Chemical Geology* **455**, 182-191

Fukao, Y., Widiyantoro, S., & Obayashi, M. (2001). Stagnant slabs in the upper and lower mantle transition region. *Reviews of Geophysics* **39**, 291-323.

Ginibre, C., Wörner, G., & Kronz, A. (2007). Crystal zoning as an archive for magma evolution. *Elements* **3**, 261-266.

Green, D. H. (2015). Experimental petrology of peridotites, including effects of water and carbon on melting in the Earth's upper mantle. *Physics and Chemistry of Minerals* **42**, 95-122.

Grégoire, M., Rabinowicz, M. & Janse, A. J. A. (2006). Mantle mush compaction: A key to understand the mechanisms of concentration of kimberlite melts and initiation of swarms of kimberlite dykes. *Journal of Petrology* **47**, 631-646.

Grützner, T., Prelević, D. & Akal, C. (2013). Geochemistry and origin of ultramafic enclaves and their basanitic host rock from Kula Volcano, Turkey. *Lithos* **180**, 58-73.

Haghipour, A., Saidi, A., Aganabati, A., Moosavi, A., Mohebi, A., Sadeghi, M. & Zarei, M. (2009). *International Geological Map of the Middle East. Commission for the Geological Map of the World (Subcommission for the Middle East)*. Geological Survey of Iran.

Hassanzadeh, J. & Wernicke, B. P. (2016). The Neotethyan Sanandaj-Sirjan zone of Iran as an archetype for passive margin-arc transitions. *Tectonics* **35**, 586-621.

Hirschmann, M. M., Kogiso, T., Baker, M. B. & Stolper, E. M. (2003). Alkalic magmas generated by partial melting of garnet pyroxenite. *Geology* **31**, 481-484.

Hofmann, A.W. (1988). Chemical differentiation of the Earth: the relationship between mantle, continental crust, and oceanic crust. *Earth and Planetary Science Letters* **90**, 297-314.

Jankovics, M. É., Taracsák, Z., Dobosi, G., Embey-Isztin, A., Batki, A., Harangi, S. & Hauzenberger, C. A. (2016). Clinopyroxene with diverse origins in alkaline basalts from the western Pannonian Basin: Implications from trace element characteristics. *Lithos* **262**, 120-134.

Kamenetsky, V. S., Kamenetsky, M. B., Sobolev, A. V., Golovin, A. V., Sharygin, V. V., Pokhilenko, N. P., & Sobolev, N. V. (2009). Can pyroxenes be liquidus minerals in the kimberlite magma? *Lithos* **112**, 213-222.

Kaviani, A., Sandvol, E., Moradi, A., Rümpker, G., Tang, Z., & Mai, P. M. (2018). Mantle transition zone thickness beneath the Middle East: evidence for segmented Tethyan slabs, delaminated lithosphere, and lower mantle upwelling. *Journal of Geophysical Research: Solid Earth* **123**, 4886-4905.

Keshav, S., Corgne, A., Gudfinnsson, G. H., Bizimis, M., McDonough, W. F., & Fei, Y. (2005). Kimberlite petrogenesis: Insights from clinopyroxene-melt partitioning experiments at 6 GPa in

the CaO-MgO-Al2O3-SiO2-CO2 system. *Geochimica et Cosmochimica Acta* **69**, 2829-2845.

Konzett, J., Sweeney, R. J., Thompson, A. B. & Ulmer, P. (1997). Potassium amphibole stability in the upper mantle: an experimental study in a peralkaline KNCMASH system to 85 GPa. *Journal of Petrology* **38**, 537–568

Larrea, P., França, Z., Lago, M., Widom, E., Galé, C. & Ubide, T. (2012). Magmatic processes and the role of antecrysts in the genesis of Corvo Island (Azores Archipelago, Portugal). *Journal of Petrology* **54**, 769-793.

Lescuyer, J. L., Riuo, R. & Babakhani, A. (1978). *Report of Ahar geological map, scale1/250000*. Geological Survey of Iran.

Lloyd, F. E., Arima, M., & Edgar, A. D. (1985). Partial melting of a phlogopite-clinopyroxenite nodule from south-west Uganda: an experimental study bearing on the origin of highly potassic continental rift volcanics. *Contributions to Mineralogy and Petrology* **91**, 321-329.

Mitchell, R. H. (1995b). The role of petrography and lithogeochemistry in exploration for diamondiferous rocks. *Journal of Geochemical Exploration* **53**, 339-350.

Mollo, S., Del Gaudio, P., Ventura, G., Iezzi, G., & Scarlato, P. (2010). Dependence of clinopyroxene composition on cooling rate in basaltic magmas: implications for thermobarometry. *Lithos* **118**, 302-312.

Morimoto, N. (1988). Nomenclature of pyroxenes. *Mineralogy and Petrology* **39**, 55-76.

Motavalli-Anbaran, S. H., Zeyen, H. & Jamasb, A. (2016). 3D crustal and lithospheric model of the Arabia-Eurasia collision zone. *Journal of Asian Earth Sciences* **122**, 158-167.

Muravyeva, N. S., Belyatsky, B. V., Senin, V. G. & Ivanov, A. V. (2014). Sr–Nd–Pb isotope systematics and clinopyroxene-host disequilibrium in ultra-potassic magmas from Toro-Ankole and Virunga, East-African Rift: Implications for magma mixing and source heterogeneity. *Lithos* **210**, 260-277.

Murphy, D. T., Collerson, K. D. & Kamber, B. S. (2002). Lamproites from Gaussberg, Antarctica: possible transition zone melts of Archaean subducted sediments. *Journal of Petrology* **43**, 981–1001.

Nimis, P. (1995). A clinopyroxene geobarometer for basaltic systems based on crystal-structure modeling. *Contributions to Mineralogy and Petrology* **121**, 115-125.

Orejana, D., & Villaseca, C. (2008). Heterogeneous metasomatism in cumulate xenoliths from the Spanish Central System: implications for percolative fractional crystallization of lamprophyric melts. *Geological Society, London, Special Publications* **293**, 101-120.

Orejana, D., Villaseca, C. & Paterson, B. A. (2007). Geochemistry of mafic phenocrysts from alkaline lamprophyres of the Spanish Central System: implications on crystal fractionation, magma mixing and xenoliths entrapment within deep magma chambers. *European Journal of*

Mineralogy **19**, 817-832.

Pang, K.-N., Chung,S.-L., Zarrinkoub, M.H., Lin,Y.-C., Lee,H.-Y., Lo, C.-H., Khatib, M.M. (2013). Iranian ultrapotassic volcanism at ~11 Ma signifies the initiation of post-collision magmatism in the Arabia-Eurasia collision zone. *Terra Nova* **25**, 405-413.

Pearce, J.A., Bender, J.F., De Long, S.E., Kidd, W.S.F., Low, P.J., Gner, Y., Saroglu, F., Yilmaz, Y.,Moorbath, S. & Mitchell, J.G. (1990).Genesis of collision volcanism in Eastern Anatolia, Turkey. *Journal of Volcanology and Geothermal Research* **44**, 189-229.

Perini, G., & Conticelli, S. (2002). Crystallization conditions of leucite-bearing magmas and their implications on the magmatological evolution of ultrapotassic magmas: the Vico Volcano, Central Italy. *Mineralogy and Petrology* **74**, 253-276.

Pilet, S. (2015). Generation of low-silica alkaline lavas: Petrological constraints, models, and thermal implications. In*:* Foulger, G. R., Lustrino, M., & King, S. D. (ed.) *The Interdisciplinary Earth: In Honor of Don L. Anderson. Geological Society of America Special Paper* **514**, 281-304.

Pilet, S., Hernandez, J. & Villemant, B. (2002). Evidence for high silicic melt circulation and metasomatic events in the mantle beneath alkaline provinces: the Na–Fe-augitic green-core pyroxenes in the Tertiary alkali basalts of the Cantal massif (French Massif Central). *Mineralogy and Petrology* **76**, 39-62.

Plank, T. & Langmuir, C. H. (1998). The chemical composition of subducting sediment and its consequences for the crust and mantle. *Chemical Geology* **145**, 325-394.

Prelević, D., Akal, C., Romer, R. L., Mertz-Kraus, R. & Helvaci, C. (2015). Magmatic response to slab tearing: Constraints from the afyon alkaline volcanic complex, Western Turkey. *Journal of Petrology* **56**, 527-562.

Prelević, D., Foley, S. F., Cvetković, V. & Romer, R. L. (2004). Origin of minette by mixing of lamproite and dacite magmas in Veliki Majdan, Serbia. *Journal of Petrology* **45**, 759-792.

Prelević, D., Foley, S. F., Romer, R., & Conticelli, S. (2008). Mediterranean Tertiary lamproites derived from multiple source components in postcollisional geodynamics. *Geochimica et Cosmochimica Acta* **72**, 2125-2156.

Putirka, K. D. (2008). Thermometers and barometers for volcanic systems. *Reviews in mineralogy and geochemistry* **69**, 61-120.

Rabinowicz, M., Ricard, Y., & Grégoire, M. (2002). Compaction in a mantle with a very small melt concentration: Implications for the generation of carbonatitic and carbonate-bearing high alkaline mafic melt impregnations. *Earth and Planetary Science Letters* **203**, 205-220.

Rapp, R. P., Irifune, T., Shimizu, N., Nishiyama, N., Norman, M. D. & Inoue, T. (2008). Subduction recycling of continental sediments and the origin of geochemically enriched reservoirs in the deep mantle. *Earth and Planetary Science Letters* **271**, 14-23.

Rhodes, J. M., Dungan, M. A., Blanchard, D. P., & Long, P. E. (1979). Magma mixing at mid-ocean ridges: evidence from basalts drilled near 22 N on the Mid-Atlantic Ridge. *Tectonophysics* **55**, 35-61.

Rigo, A., Adam, C., Grégoire, M., Gerbault, M., Meyer, R., Rabinowicz, M. & Bonvalot, S. (2015). Insights for the melt migration, the volcanic activity and the ultrafast lithosphere delamination related to the Yellowstone plume (Western USA). *Geophysical Journal International* **203**, 1274-1301.

Rock, N.M.S. (1991). *Lamprophyres*. Glasgow: Blackie, pp. 285.

Rosenbaum, G., Gasparon, M., Lucente, F. P., Peccerillo, A., & Miller, M. S. (2008). Kinematics of slab tear faults during subduction segmentation and implications for Italian magmatism. *Tectonics* **27**, 1-16.

Sato, K. (1997). Melting experiments on a synthetic olivine lamproite composition up to 8 GPa: implication to its petrogenesis. *Journal of Geophysical Research: Solid Earth* **102**, 14751-14764.

Semiz, B., Çoban, H., Roden, M. F., Özpınar, Y., Flower, M. F. & McGregor, H. (2012). Mineral composition in cognate inclusions in Late Miocene-Early Pliocene potassic lamprophyres with affinities to lamproites from the Denizli region, Western Anatolia, Turkey: implications for uppermost mantle processes in a back-arc setting. *Lithos* **134**, 253-272.

Soltanmohammadi, A. (2018). Sources of the alkaline magmatism in the Turkish-Iranian Plateau: a link with the dynamic of stagnant lithospheres within the Mantle Transition Zone. *Ph.D. thesis, Université Toulouse 3 Paul Sabatier (UT3 Paul Sabatier)*, 285 pp.

Soltanmohammadi, A., Grégoire, M., Rabinowicz, M., Gerbault, M., Ceuleneer, G., Rahgoshay, M., Bystricky, M. & Benoit, M. (2018). Transport of volatile-rich melt from the mantle transition zone via compaction pockets: implications for mantle metasomatism and the origin of alkaline lavas in the Turkish–Iranian Plateau. *Journal of Petrology* **59**, 2273-2310.

Spera, F. J. (1987). Dynamics of translit+hospheric migration of metasomatic fluid and alkaline magma. In: Menzies, M. & Hawkesworth, C. J. (eds) Mantle Metasomatism. London: Academic Press, 1-19.

Stampfli, G.M. (2000). Tethyan oceans. In: Bozkurt, E., Winchester, J.A., Piper, J.D.A. (Eds.), Tectonics and magmatism in Turkey and the surrounding area. *Geological Society of London, Special Publication* **173**, 163-185.

Streck, M.J. (2008). Mineral textures and zoning as evidence for open system processes. *Reviews in Mineralogy and Geochemistry* **69**, 595-622.

Sun, S. S. & McDonough, W. S. (1989). Chemical and isotopic systematics of oceanic basalts: implications for mantle composition and processes. *Geological Society, London, Special Publications* **42**, 313-345.

Tappe, S. (2004). Mesozoic mafic alkaline magmatism of southern Scandinavia. *Contributions to*

Mineralogy and Petrology **148**, 312-334.

Ubide, T., & Kamber, B. S. (2018). Volcanic crystals as time capsules of eruption history. *Nature communications* **9**, 1-12.

Ubide, T., Galé, C., Larrea, P., Arranz, E. & Lago, M. (2014). Antecrysts and their effect on rock compositions: the Cretaceous lamprophyre suite in the Catalonian Coastal Ranges (NE Spain). *Lithos* **206**, 214-233.

Ubide, T., Mollo, S., Zhao, J. X., Nazzari, M., & Scarlato, P. (2019). Sector-zoned clinopyroxene as a recorder of magma history, eruption triggers, and ascent rates. *Geochimica et Cosmochimica Acta* **251**, 265-283.

Veizer, J. (1989). Strontium isotopes in seawater through time. *Annual Review of Earth and Planetary Sciences* **17**, 141-167.

Vincent, S. J., Allen, M. B., Ismail-zadeh, A. D., Foland, K. A. & Simmons, M. D. (2005). Insights from the Talysh of Azerbaijan into the Paleogene evolution of the South Caspian region, *Geological Society of America Bulletin* **11/12**, 1513-1533.

Wagner, C., & Velde, D. (1986). The mineralogy of K-richterite-bearing lamproites. *American Mineralogist* **71**, 17-37.

Wang, Y. and Foley, S.F. (2018). Hybridization melting between continent-derived sediment and depleted peridotite in subduction zones. *Journal of Geophysical Research: Solid Earth*, **123**, 3414-3429.

Weaver, B. L. (1991). The origin of ocean island basalt end-member compositions: trace element and isotopic constraints. *Earth and Planetary Science Letters* **104**, 381-397.

Zhu, Y. & Ogasawara, Y. (2004). Clinopyroxene phenocrysts (with green salite cores) in trachybasalts: implications for two magma chambers under the Kokchetav UHP massif, North Kazakhstan. *Journal of Asian Earth Sciences* **22**, 517-527.

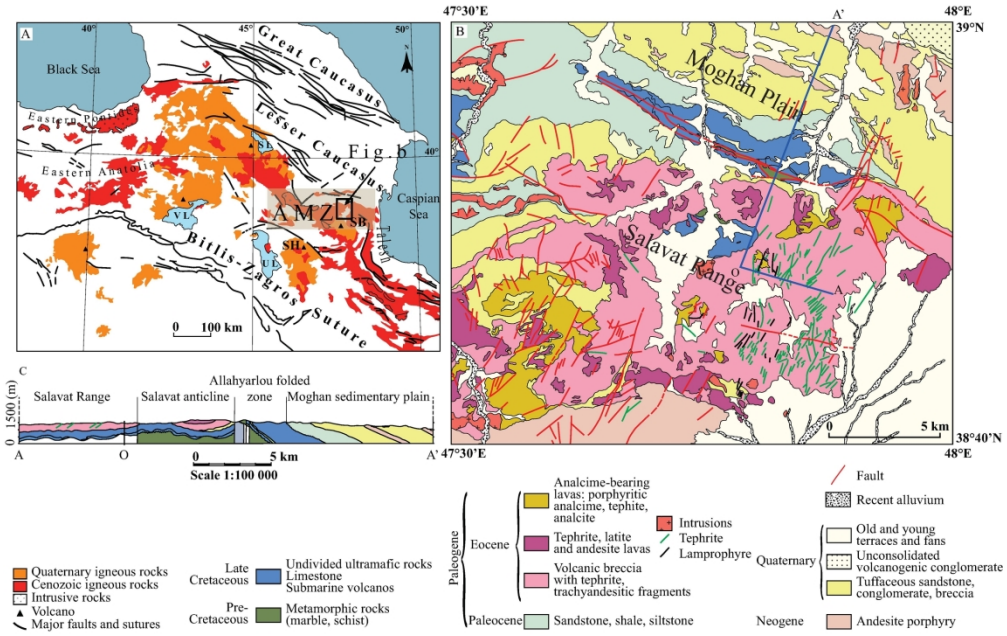

Fig. 1 (a) Simplified geological map covering Cenozoic–Quaternary magmatism from East Anatolia to NW Iran (modified from Haghipour et al. (2009)). (b) Geological map showing the distribution of Cenozoic magmatism in the Salavat Range (modified after Babakhani et al., 1990). (c) Cross-section (A–A') from the north to the centre of the Salavat Range. Key features: AMZ: Azerbaijan magmatic zone; UL Urmieh Lake; VL, Van Lake; SV, Sevan Lake; Quaternary volcanoes (triangles); SH, Sahand; SB, Sabalan.

212x158mm (300 x 300 DPI)

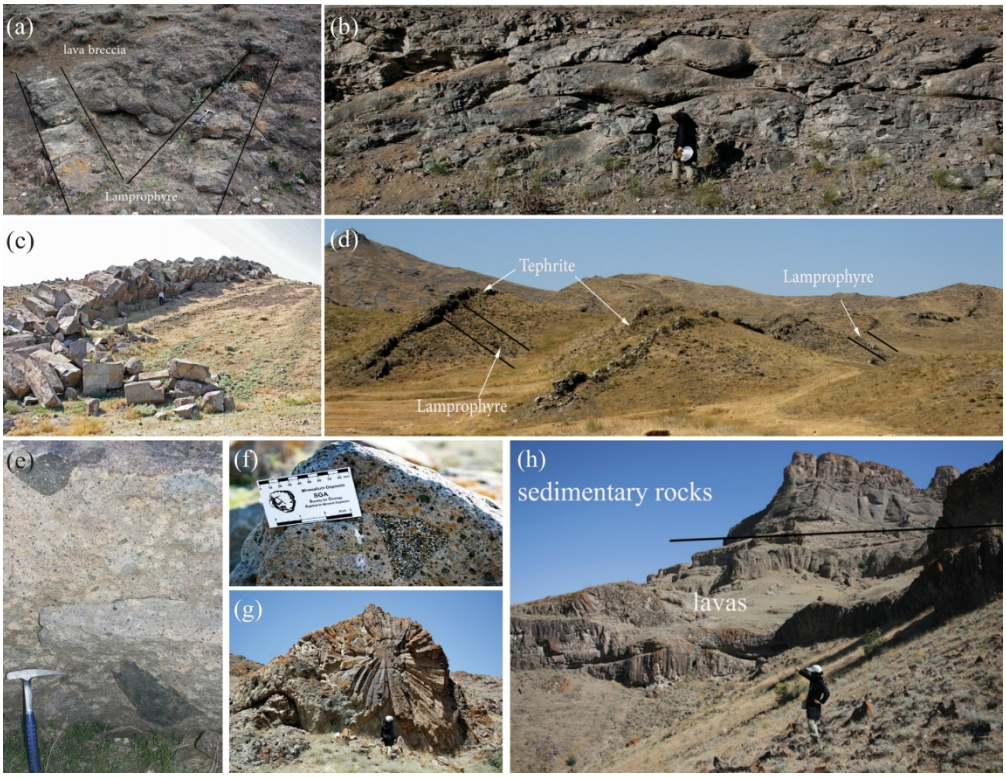

Fig. 2 Field photographs showing outcrops of (a) lamprophyre dykes that cross-cut the volcanic breccia and pillow lavas. (b) Pillow structures vary in shape and size. (c) Tephrite dykes contain horizontal columnar joint structures. (d) Tephrite dykes cross-cut both lamprophyre and volcanic breccia. (e) Ultramafic and (f) mafic cumulative xenoliths are hosted by lamprophyres. Analcime-bearing lavas display (g) columnar joint structures covered by Oligocene–Miocene sedimentary rocks (h).

170x130mm (300 x 300 DPI)

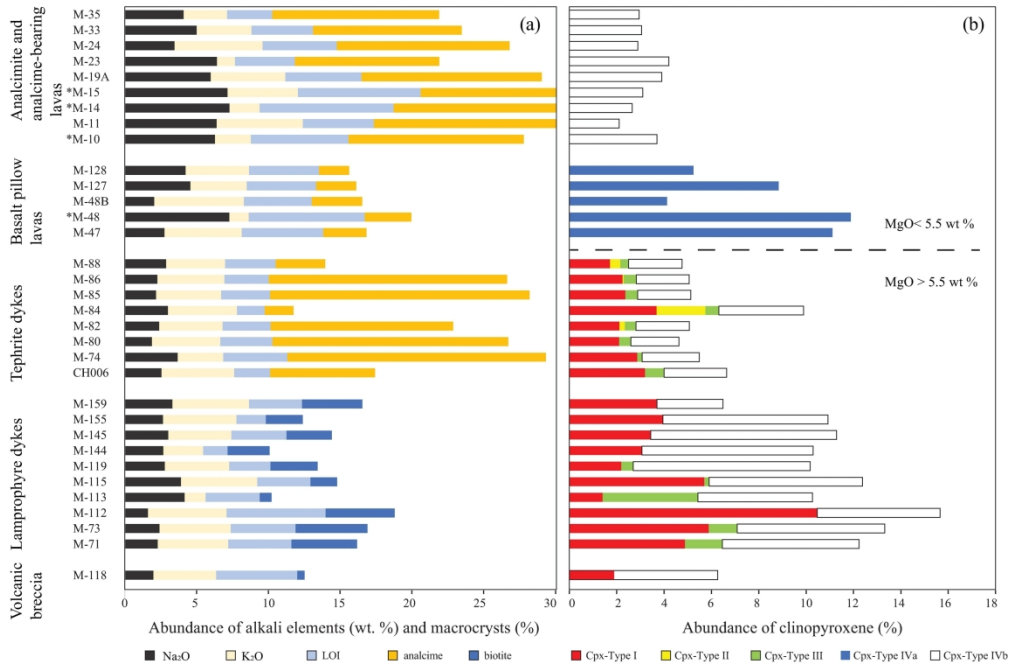

Fig. 3 Histograms comparing (a) the modal abundance of mineral assemblages, alkali elements and LOI contents and (b) various zoned clinopyroxenes of igneous rocks collected from the Salavat Range. The symbol * indicates that sample has been considered to be affected by alteration.

256x175mm (300 x 300 DPI)

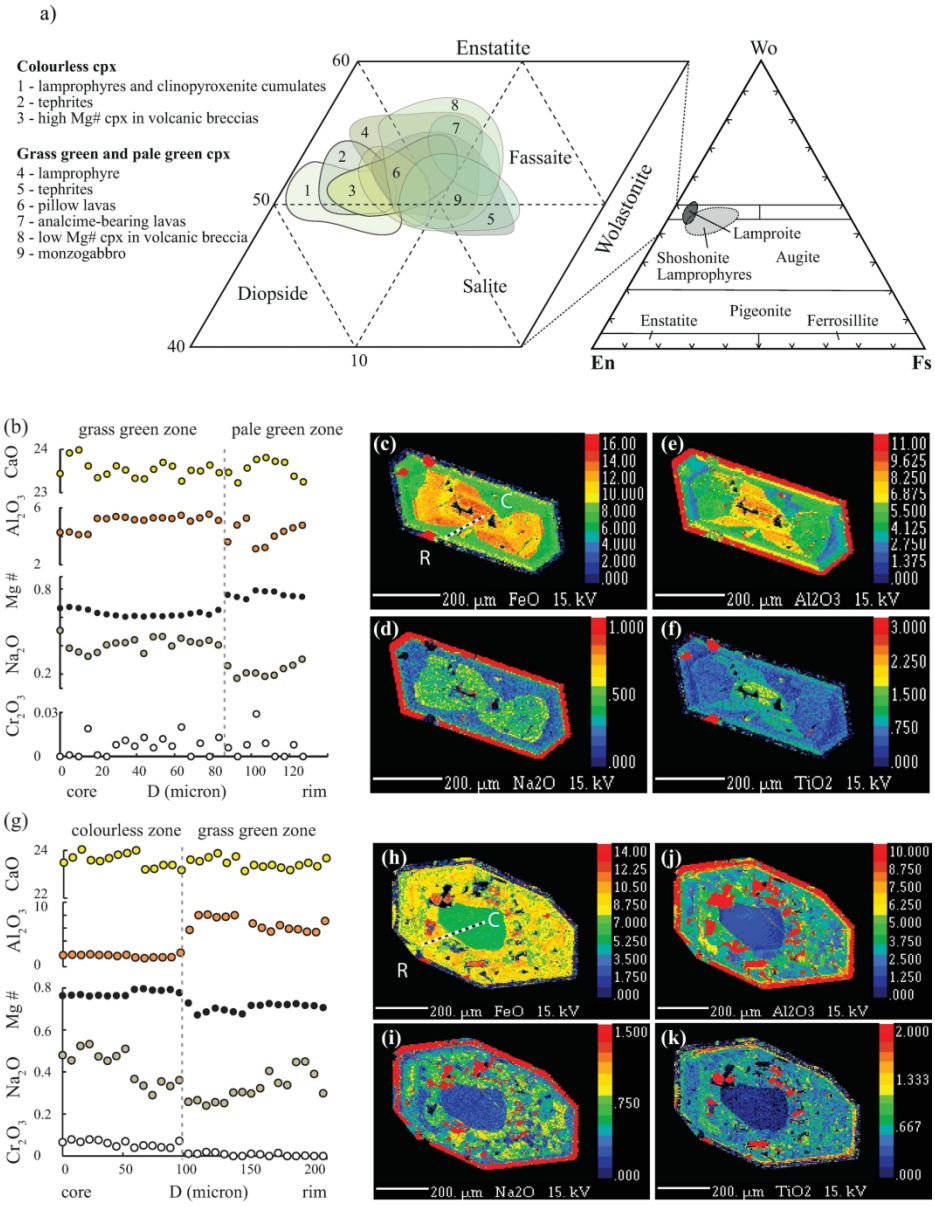

Fig. 4 (a) Chemical classification (Mg–Ca–Fe mol%) diagrams for colourless and green-zoned clinopyroxenes from the studied lavas (after Morimoto, 1988); compositional fields of lamproites and lamprophyres after Rock (1991). (b–k) Variation in major elements from core to rim (C–R line in c) in grass green (Type-III) zoned clinopyroxenes from kersantite.

184x237mm (300 x 300 DPI)

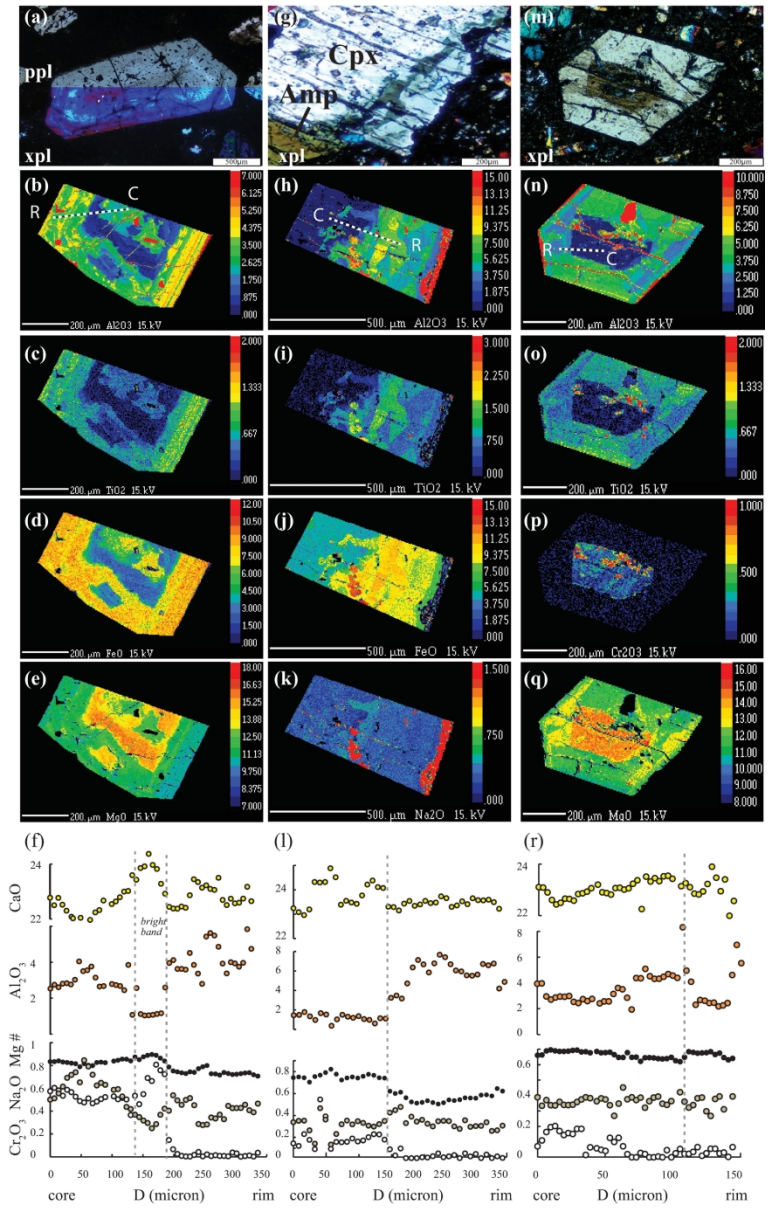

Fig. 5 Variation in major elements from core to rim (C–R line in b) in colourless (Type-II) clinopyroxene from tephrite dykes (a–f), as well in (g–l) colourless (Type-I) zoned clinopyroxenes from clinopyroxenite cumulates and (m–r) kersantite.

168x266mm (300 x 300 DPI)

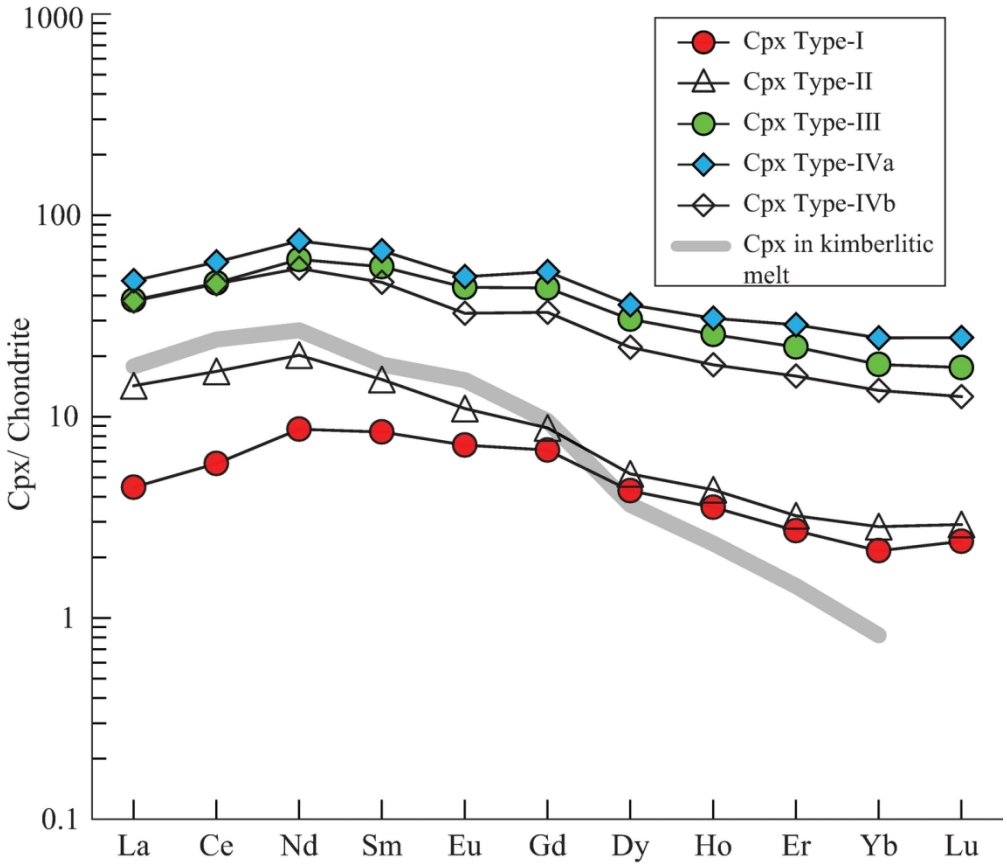

Fig. 6 Diagrams presenting the average concentration of trace elements in different zoned clinopyroxenes normalized to chondrite (Sun & McDonough, 1989). REE concentrations of clinopyroxenes from kimberlite are from Kamenetsky et al. (2009).

135x116mm (300 x 300 DPI)

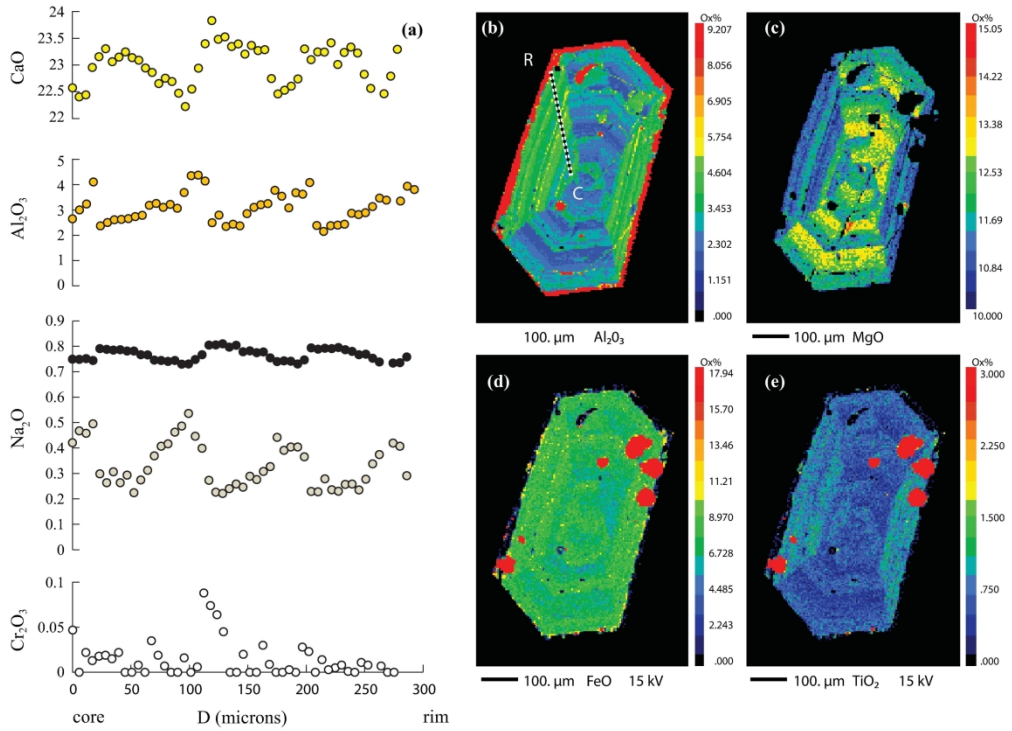

Fig. 7 Variation in major elements from core to rim (C–R line in b) in oscillatory-sectored zoned clinopyroxenes (Type-IVb) from tephrite.

228x165mm (300 x 300 DPI)

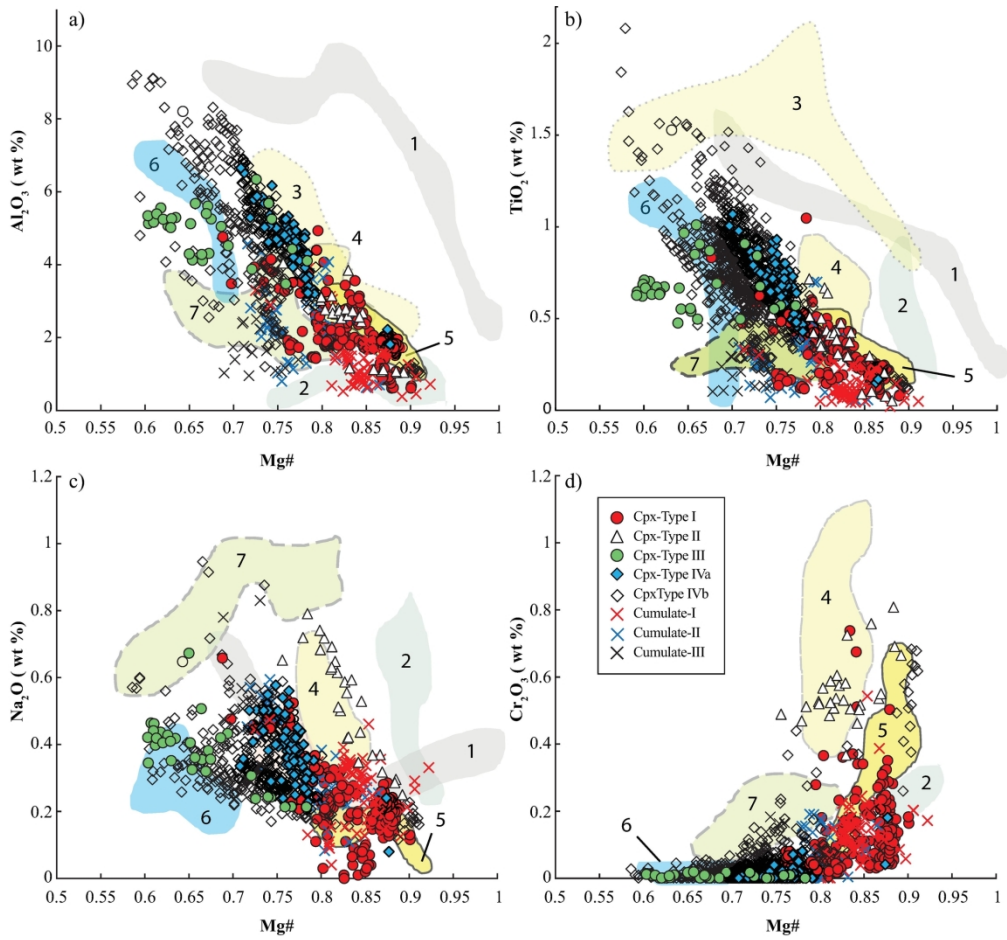

Fig. 8 (a–d) Variation in major elements among the types of zoned clinopyroxenes. Fields marked by numbers are representative compositions of clinopyroxenes from worldwide alkaline magmatism: 1) colourless clinopyroxene from Vulsini, Italy (Barton et al., 1982); (2) cumulative xenoliths from Spain (Orejana & Villaseca, 2008) and Turkey (Semiz et al., 2012); colourless clinopyroxenes from Leucite Hill (Barton & van Bergen, 1981); (3) cumulative xenoliths, Turkey (Semiz et al., 2012), lamprophyres, Iran (Aghazadeh et al., 2015); (4) Mg-rich clinopyroxenes from lamprophyres, Spain (A-type in Ubide et al., 2014); (5) colourless clinopyroxenes, Kazakhstan (Zhu & Ogasawara, 2004); (6) green clinopyroxenes, Kazakhstan (Zhu & Ogasawara, 2004); (7) green clinopyroxenes from Leucite Hill (Barton & van Bergen, 1981).

201x187mm (300 x 300 DPI)

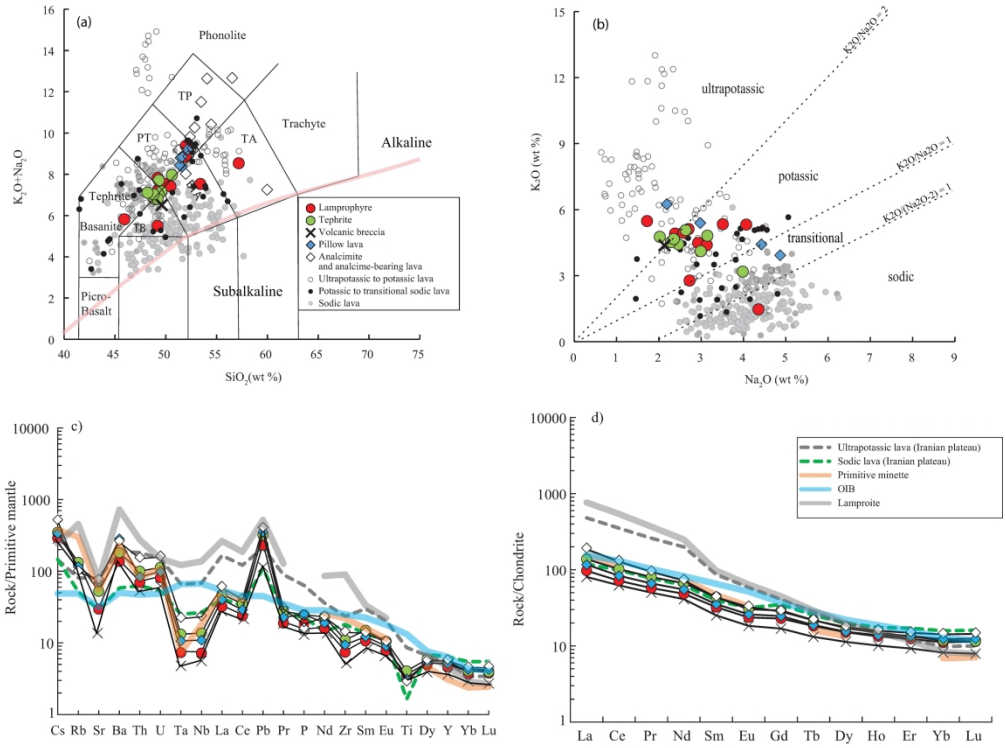

Fig. 9 (a) Total alkali vs silica diagram (Le Maître, 2002); (b) K2O vs Na2O diagram for the classification of the studied rocks. The data for alkaline lavas from the Turkish-Iranian plateau are from the literature (see references in Soltanmohammadi et al., 2018) Patterns of (c) whole-rock trace elements and (d) REE normalized to the primitive mantle and chondrite values (Sun & McDonough, 1989). The values in figures c and d are mean compositions for different category of rock samples. Other reference sources are oceanic island basalt (OIB; Sun & McDonough 1989), primitive minette (Buhlmann et al., 2000) and lamproites derived from the mantle transition zone (Murphy et al., 2002).

287x212mm (300 x 300 DPI)

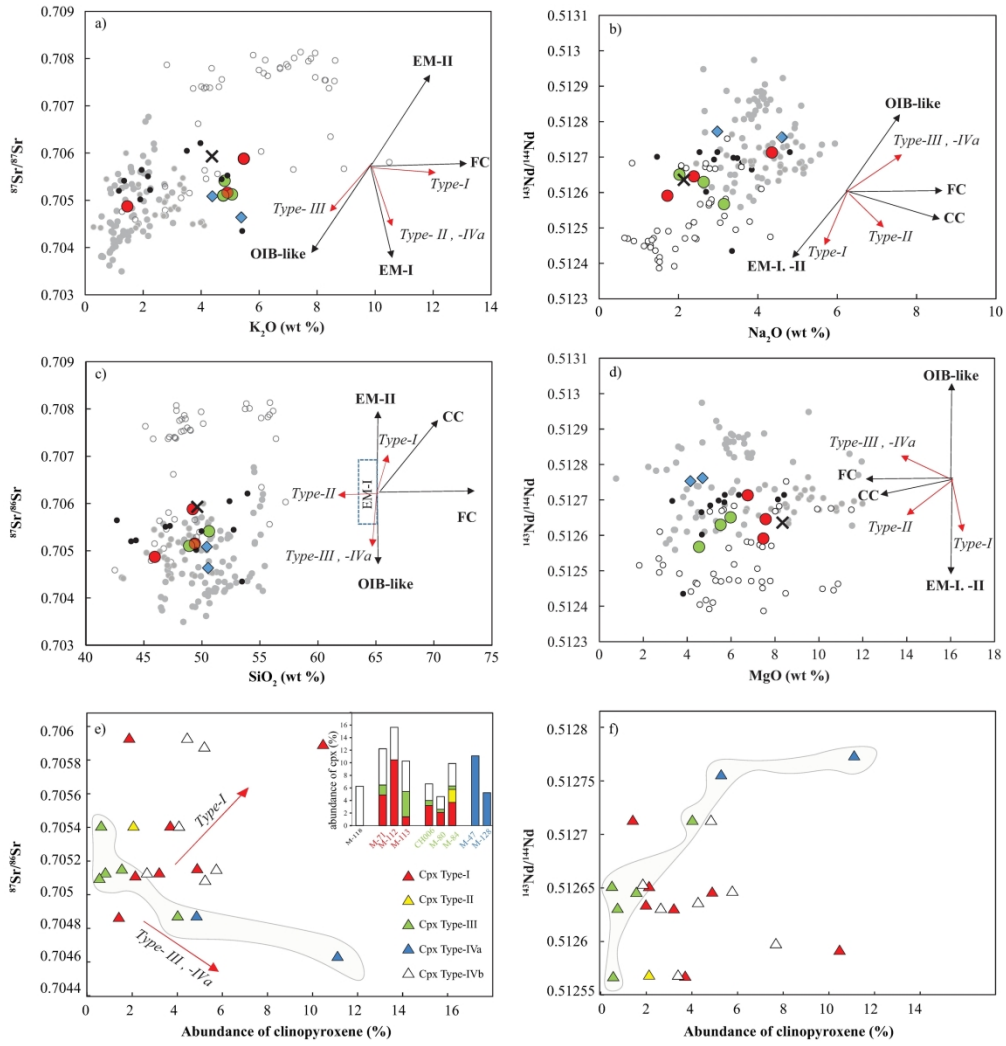

Fig. 10 Whole-rock Sr–Nd isotope ratios vs whole rock major elements (wt %) (a–d) and modal abundance of different types of clinopyroxene (e–f) for the studied lavas. The red arrows in figures a–d are derived from figures e–f and reflect the increasing mode of the various types of zoned clinopyroxenes in different rock types; symbols are as in Fig. 9a. The black arrow estimates the change of composition related to mantle sources (OIB, EM-I and -II), continental crust (CC) and fractional crystallization (FC). The alkaline lavas from the Turkish-Iranian plateau are plotted for comparison purposes. (e and f) The grey fields show the correlation between modal abundance of crystal types- III and -IVa and the whole-rock Sr and Nd isotopic compositions of different kind of rock types presented in figures a-d.

284x294mm (300 x 300 DPI)

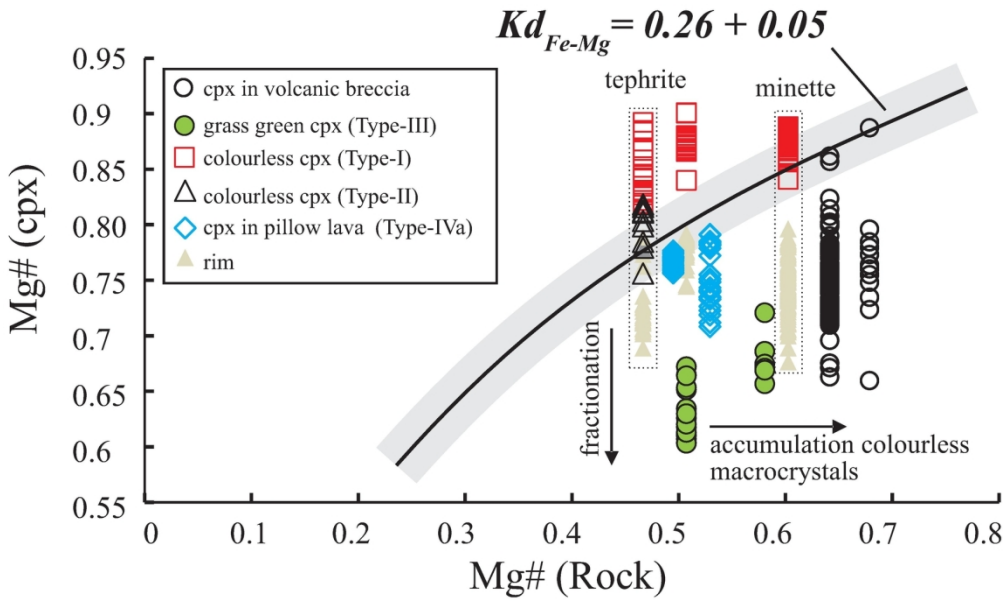

Fig. 11 Mg# in clinopyroxene (cpx) vs Mg# in a whole-rock diagram. The black curve represents the mineral-melt equilibrium according to the Fe–Mg exchange (after Rhodes et al., 1979) using the distribution coefficient (KdFe–Mg = 0.26 ± 0.05) of Aknin et al. (2005).

157x94mm (300 x 300 DPI)

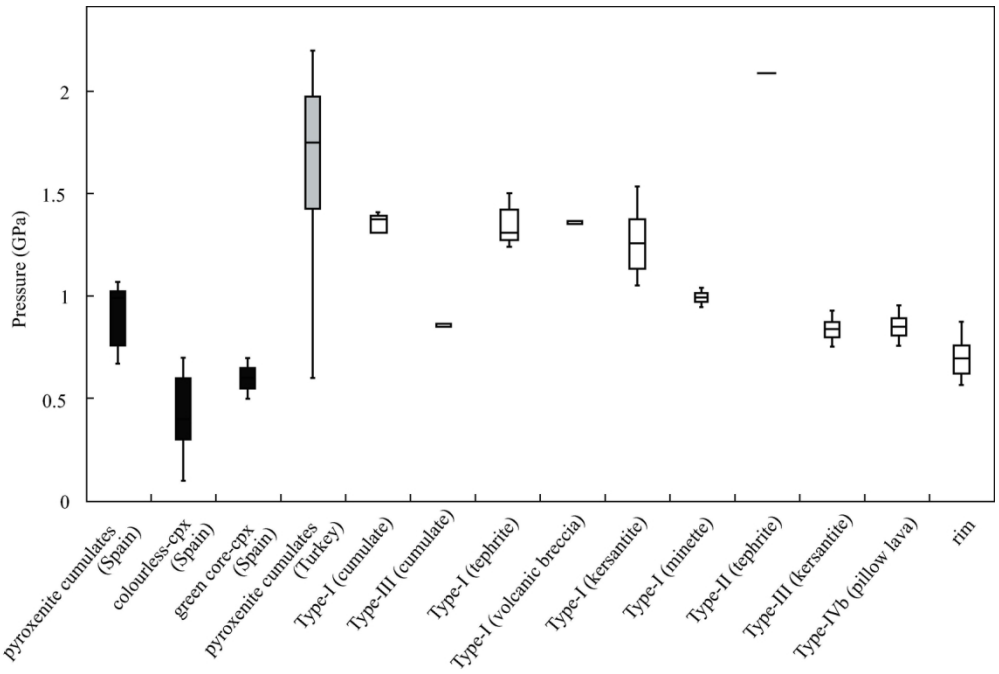

Fig. 12 Pressure of crystallization estimated for different types of zoned clinopyroxenes from the studied lavas and cumulative xenoliths. For comparison, the pressure of mineral crystallization for cumulative xenoliths hosted in similar alkaline lavas are presented; these latter samples are from Spain (Orejana & Villaseca, 2008) and Turkey (Prelević et al., 2015; Semiz et al., 2012).

144x96mm (300 x 300 DPI)

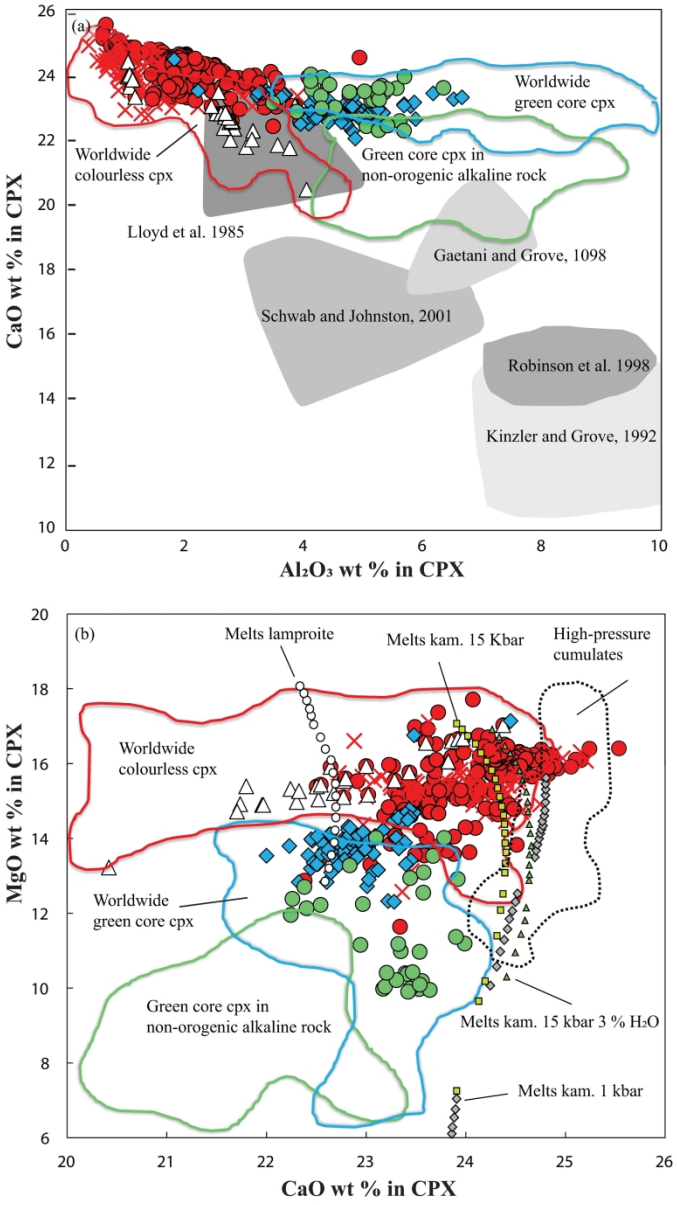

Fig. 13 CaO vs (a) Al2O3 and (b) MgO contents (wt %) in colourless (Types-I and -II), grass green (Type-III) zoned clinopyroxenes from cumulative xenoliths and lavas from this study; symbols are as in Fig. 8. Worldwide green clinopyroxenes are from Spain (Orejana et al., 2007; low MgO zoned clinopyroxenes from Ubide et al., 2014); Leucite Hill, Wyoming (Barton & van Bergen, 1981) and Kazakhstan (Zhu & Ogasawara, 2004). Colourless clinopyroxenes are also from the above-mentioned references with the addition of cumulates from Turkey (Semiz et al., 2012) and high-MgO zoned clinopyroxene from Ubide et al. (2014). Green clinopyroxene hosted in non-orogenic alkaline rocks are from Massif Central (Pilet et al., 2002) and Eifel (Duda & Schmincke, 1985). The shaded field in (a) is clinopyroxene content from different experimental studies, modified after Semiz et al. (2012). In (b), the high-pressure cumulative xenolith from Turkey and MELTS calculations at various crystallization pressures for exotic melts (e.g. kamafugite and lamproites) at fixed water contents of 1 and 2 wt % are from Prelević et al., 2015.

192x344mm (300 x 300 DPI)

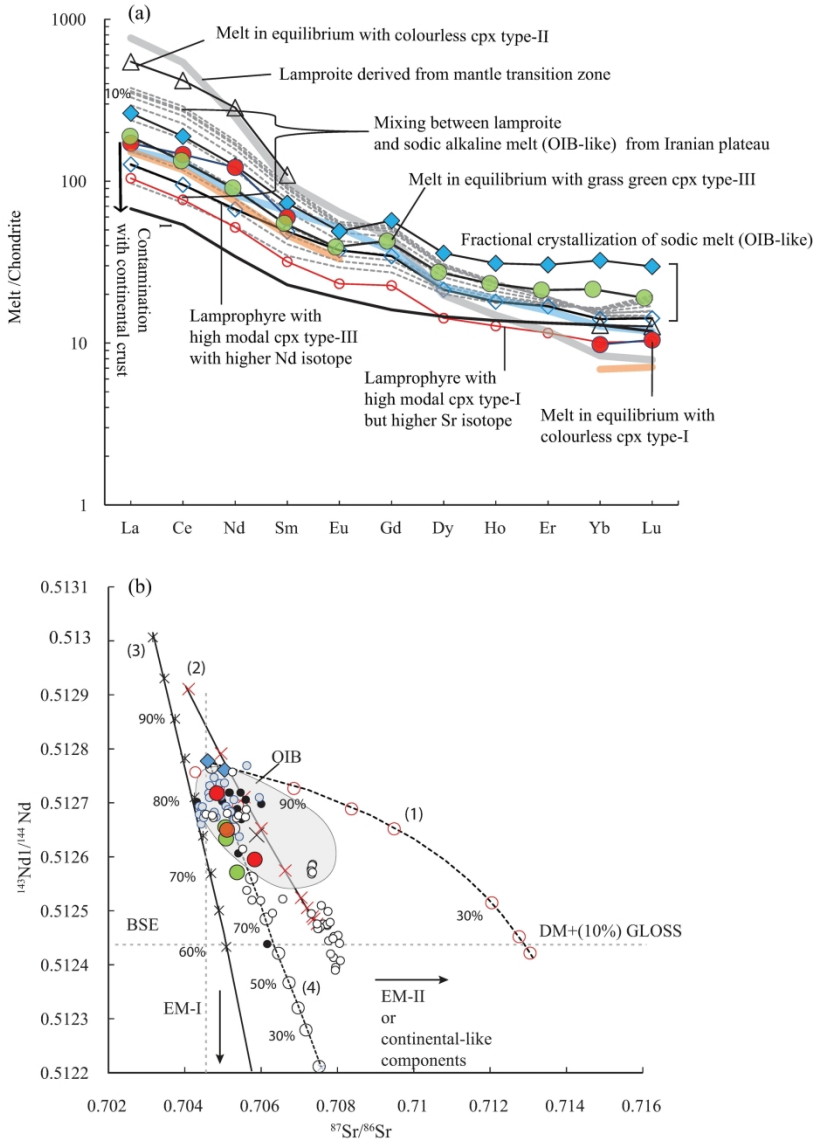

Fig. 14 (a) Diagram presenting REE concentrations of ultrapotassic and sodic alkaline lavas from the plateau and REE concentrations of theoretical melts in equilibrium with colourless (Type-I and-II), grass green (Type-III) and pale green (Type-IVa) clinopyroxenes (symbols as in Fig. 6). Melt calculations are based on Kd mineral-melt, as proposed by Keshav et al. (2005) for exotic melts in equilibrium with colourless clinopyroxene, whereas green clinopyroxene partition coefficients are from Ubide et al. (2014). In this diagram, results are compared with whole-rock samples having the highest modes of colourless clinopyroxene and green core clinopyroxene, respectively. Dashed lines represent the mixing of averaged lamproites and OIB-like melts from the Turkish-Iranian plateau. The continental crust average is from Hofmann (1988). References for OIB, primitive minette and lamproites are the same as in Fig. 9. (b) A 143Nd/144Nd vs 87Sr/86Sr diagram illustrating the 4 mixing lines between the different endmembers; see text for detail of endmembers used to calculated mixing lines. Symbols are as in Fig. 9a.

197x286mm (300 x 300 DPI)

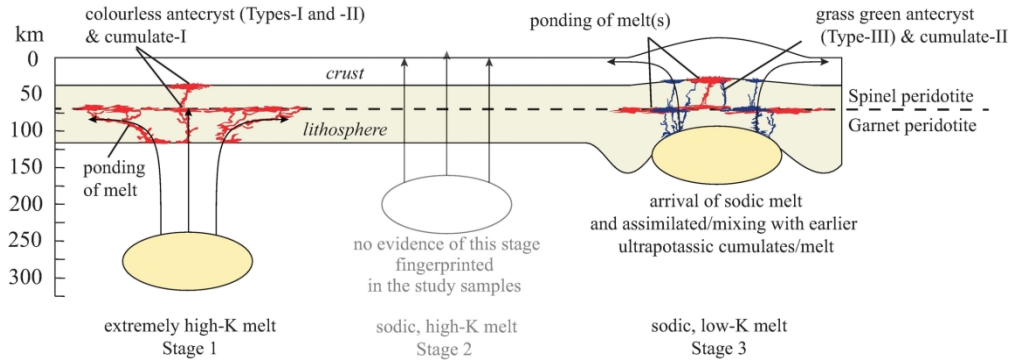

Fig. 15. Simplified schematic diagram showing the three stages of the ascent of compaction pockets through the upper mantle and the associated melt compositions, as proposed by Soltanmohammadi et al. (2018). According to the mineral and whole-rock chemistry of the lavas, the geochemical characteristics of the melts extracted from Stage 1 (ultrapotassic) and Stage 3 (sodic) explain the formation of the various cumulates and both types of antecrystals, colourless and grass green antecrystals, hosted in the studied lavas.

186x66mm (300 x 300 DPI)

Table, 1 whole rock major (%), trace elements (ppm) of studied rock from the Salavat Range,

Sample	M-118	M-71	M-73	M-112	M-113	M-115
Rock type	*Volcanic breccias*	*Lamprophyr*	*Lamprophyr*	*Lamprophyr*	*Lamprophyr*	*Lamprophyr*
(wt%)						
SiO_2	46.5	47.6	46.9	46.3	44.1	50.1
TiO_2	0.69	0.77	0.74	0.71	0.92	0.73
Al_2O_3	11.5	13.5	13.25	13	15.05	15.5
Fe_2O_3	8.66	10.45	9.93	9.19	12.5	9.45
MnO	0.15	0.17	0.16	0.15	0.22	0.16
MgO	7.82	7.3	6.58	7.03	6.49	5.85
CaO	11.8	9.01	8.93	10.4	10.35	5.02
Na_2O	2	2.3	2.43	1.62	4.18	3.92
K_2O	4.1	4.73	4.66	5.15	1.4	5.12
P_2O_5	0.31	0.31	0.3	0.33	0.59	0.33
BaO	0.11	0.13	0.11	0.11	0.1	0.11
LOI	5.64	4.41	4.52	6.9	3.77	3.7
Total	99.39	100.76	98.59	100.96	99.76	100.03
(ppm)						
Sc	36.79	42.58	41.86	40.71	59.26	26.90
V	254.45	301.24	289.43	248.19	395.70	305.66
Cr	380.11	121.44	135.11	157.37	34.34	43.06
Co	34.71	34.43	33.48	35.17	37.04	25.46
Ni	146.26	25.93	28.17	55.51	15.46	19.89
Cu	96.67	110.58	124.23	104.73	156.44	86.14
Zn	68.63	72.23	64.26	67.87	105.07	65.34
Rb	74.06	109.14	90.33	106.18	24.93	85.24
Sr	298.94	617.33	780.47	609.77	756.66	494.03
Y	17.88	22.05	22.10	20.56	31.22	22.89
Zr	60.66	72.55	71.05	85.67	81.54	120.97
Nb	4.36	4.13	4.29	7.47	5.28	7.10
Mo	0.57	0.39	1.42	0.46	0.32	0.45
Sn	0.72	1.00	1.36	1.17	1.30	
Cs	2.16	3.21	1.86	0.75	3.56	7.05
Ba	959.58	1155.97	996.44	931.10	927.39	909.17
La	19.41	22.38	21.82	24.68	30.07	18.32
Ce	39.14	43.25	42.49	47.05	58.17	35.65
Pr	4.87	5.34	5.36	5.90	7.41	4.40
Nd	19.50	22.32	22.44	24.20	31.32	18.76
Sm	4.02	4.98	4.87	4.86	7.47	4.26
Eu	1.17	1.44	1.39	1.35	2.17	1.06
Gd	3.85	4.77	4.60	4.65	7.08	3.98
Tb	0.54	0.70	0.69	0.66	0.96	0.65
Dy	3.19	3.85	3.85	3.62	5.42	3.85
Ho	0.62	0.74	0.74	0.72	1.02	0.79
Er	1.65	2.05	2.06	1.91	2.79	2.16
Yb	1.49	1.83	1.84	1.72	2.39	2.06
Lu	0.21	0.28	0.27	0.26	0.36	0.34
Hf	1.60	1.81	1.88	2.21	2.09	2.66
Ta	0.21	0.25	0.30	0.43	0.26	0.40
W	0.44	0.37	2.06	0.32	1.07	2.32
Pb	8.35	15.94	14.25	17.06	21.00	7.39
Th	4.46	5.30	5.81	5.34	7.59	5.72
U	1.25	1.49	1.54	1.54	1.71	1.80
Eu/Eu*	0.91	0.90	0.90	0.87	0.91	0.78

La/Yb (n)	9.34	8.76	8.52	10.31	9.03	6.37
Nb/La (n)	0.22	0.18	0.19	0.29	0.17	0.37

* The sample has been considered to be affected by alteration.

M-119	M-144	M-159	M-145	M-155	CH006B	M-74	M-80
Lamprophyr	*Lamprophyr*	*Lamprophyr*	*Lamprophyr*	*Lamprophyre*	*Tephrite*	*Tephrite*	*Tephrite*
48.2	48.5	49.1	51.8	48.6	47.9	45.9	45.9
0.75	0.96	0.63	0.7	0.86	0.84	0.72	0.76
13.85	17.15	15.4	15.5	15.15	14.85	13.35	14
9.89	11	8.42	9.19	11.25	10.7	9.92	10.1
0.15	0.19	0.17	0.12	0.19	0.18	0.17	0.17
6.81	5.47	5.43	5.78	5.37	5.36	5.98	5.61
8.25	9.3	6.38	6.07	8.78	8.9	9.09	10.15
2.8	2.69	3.32	3.04	2.67	2.56	3.69	1.9
4.28	2.73	5.04	4.26	5.05	4.92	2.94	4.47
0.31	0.39	0.36	0.33	0.58	0.57	0.53	0.51
0.11	0.1	0.11	0.11	0.13	0.17	0.15	0.14
2.87	1.7	3.7	3.84	2.05	2.5	4.47	3.63
98.38	100.3	98.15	100.83	100.81	99.57	97.1	97.5
37.32	33.39	25.20	26.20	28.64	29.75	29.39	29.62
270.71	332.63	252.13	240.34	331.62	326.86	377.44	303.55
107.04	24.44	66.45	31.31	29.21	53.61	44.67	67.63
31.13	31.36	24.09	23.42	30.63	29.68	30.46	33.00
23.40	18.01	18.37	21.94	20.65	22.39	21.05	23.00
109.70	151.48	104.37	88.91	114.90	101.44	500.67	125.99
62.63	88.12	77.75	57.60	82.98	77.58	77.56	90.40
87.46	62.86	103.32	74.08	107.52	86.90	80.02	93.64
642.76	678.06	1080.63	470.91	1001.25	1038.59	1112.46	1074.39
22.67	22.43	24.47	21.01	25.20	24.44	23.66	25.00
71.24	85.37	97.30	84.89	159.86	147.15	131.02	115.98
4.49	6.33	6.28	4.80	13.25	11.93	8.10	9.61
0.86	0.56	0.80	1.02	2.40	1.87	0.74	0.80
1.00	1.32	1.26	1.07				1.46
1.16	2.70	3.09	0.44	1.92	2.85	3.02	1.71
939.65	875.89	1031.39	911.53	1046.12	1083.86	1303.68	1309.59
22.29	33.72	31.01	18.10	33.10	30.67	30.32	33.46
43.10	60.96	56.95	35.27	64.18	60.00	59.28	64.50
5.43	7.06	6.77	4.23	7.91	7.38	7.28	7.85
21.83	28.02	27.03	17.70	32.39	30.50	30.40	32.09
4.79	5.99	5.42	4.07	6.75	6.38	6.41	6.92
1.27	1.72	1.50	1.16	1.69	1.54	1.54	1.90
4.60	5.26	5.24	3.81	5.45	5.45	5.45	6.57
0.69	0.75	0.73	0.59	0.81	0.81	0.77	0.85
3.78	4.01	4.07	3.47	4.34	4.08	4.16	4.54
0.77	0.77	0.81	0.70	0.84	0.82	0.78	0.87
1.99	2.12	2.23	2.06	2.19	2.12	2.08	2.15
1.99	1.86	2.22	1.96	2.01	1.94	1.86	2.01
0.28	0.27	0.36	0.29	0.32	0.30	0.28	0.29
1.97	2.16	2.19	2.19	3.44	3.13	2.82	2.83
0.23	0.41	0.36	0.32	0.76	0.59	0.43	0.53
0.91	0.42	0.84	1.88	5.04	2.45	0.90	1.07
15.03	29.60	30.22	12.04	14.29	12.66	16.80	25.73
5.94	10.80	7.69	5.53	8.44	7.54	8.14	8.23
1.81	2.87	2.27	1.66	2.46	2.22	2.10	2.24
0.83	0.94	0.86	0.90	0.85	0.80	0.80	0.86

8.02	13.01	10.00	6.61	11.84		11.32	11.69	11.94
0.19	0.18	0.19	0.26	0.39		0.37	0.26	0.28

M-82	M-84	M-85	M-86	M-88	M-47	*M-48	M-48B
Tephrite	*Tephrite*	*Tephrite*	*Tephrite*	*Tephrite*	*Pillow lavas*	*Pillow lavas*	*Pillow lavas*
47.6	48.4	47.1	47.2	46.6	48	48.4	48.4
0.8	0.89	0.78	0.78	0.78	0.66	0.66	0.68
14.6	15.2	14.3	14.65	14.65	16.9	17.4	17
10.6	9.83	10.25	10.4	10.65	7.7	7.56	7.92
0.18	0.16	0.18	0.18	0.18	0.18	0.19	0.19
5.8	4.34	5.72	5.83	6.15	4.37	3.53	4.54
10.35	8.45	10.05	10	9.93	6.45	5.88	6.62
2.4	3.01	2.19	2.28	2.89	2.77	7.29	2.06
4.31	4.6	4.33	4.51	3.97	5.01	1.25	5.88
0.57	0.45	0.54	0.56	0.56	0.55	0.51	0.53
0.15	0.15	0.14	0.15	0.15	0.21	0.1	0.2
3.35	1.93	3.42	3.09	3.53	5.68	8.08	4.72
100.86	97.49	99.11	99.77	100.13	98.65	100.96	98.85
29.03	26.10	37.79	28.81	33.17	13.27	14.31	15.46
286.96	270.06	279.60	283.82	275.44	279.25	288.54	265.71
45.95	27.38	57.40	62.01	76.32	14.05	13.73	14.94
32.32	29.41	31.75	32.25	34.33	20.54	21.44	23.05
21.72	13.40	21.65	22.06	22.53	6.97	6.61	7.52
123.39	123.58	121.51	123.37	154.47	111.38	120.52	128.83
87.31	87.90	87.22	84.82	83.89	82.19	89.68	94.97
77.84	103.08	91.35	83.85	57.82	89.77	32.47	94.57
1099.70	1088.91	1171.68	1089.74	1157.76	1609.59	392.42	1254.01
24.58	28.69	27.86	24.24	20.46	21.96	22.68	24.46
113.38	147.54	121.16	112.08	98.14	95.40	104.65	108.53
9.71	12.73	9.08	8.97	8.31	5.67	7.90	8.30
0.87	1.86	0.89	1.01	0.71	0.40	1.20	0.17
1.44	1.90	1.41	1.57	1.16		1.10	1.58
2.96	4.73	1.98	3.53	1.31	2.00	3.86	1.69
1285.80	1316.20	1327.67	1237.46	1273.68	1634.04	877.84	1747.42
32.92	35.75	33.33	32.01	32.82	26.02	26.97	28.04
62.77	68.90	64.02	61.38	59.45	47.72	50.68	52.07
7.55	8.21	7.97	7.52	7.21	5.83	6.10	6.46
31.45	32.61	32.63	31.45	28.44	23.65	25.10	26.96
6.60	7.12	7.10	6.84	5.94	4.85	5.49	5.70
1.90	1.84	1.95	1.81	1.62	1.20	1.53	1.61
6.13	6.57	6.50	6.03	5.26	4.39	4.99	5.29
0.83	0.91	0.85	0.79	0.71	0.63	0.68	0.74
4.38	5.05	4.73	4.22	3.72	3.48	3.86	4.09
0.85	0.99	0.88	0.81	0.72	0.71	0.75	0.83
2.31	2.63	2.39	2.19	1.83	1.99	2.09	2.40
1.99	2.49	2.11	1.90	1.63	1.90	2.05	2.19
0.30	0.34	0.31	0.28	0.24	0.30	0.30	0.32
2.61	3.36	2.99	2.70	2.11	1.74	2.37	2.57
0.52	0.72	0.55	0.54	0.46	0.25	0.42	0.51
0.78	1.82	0.98	0.36	0.89	0.95	1.49	0.30
24.55	25.12	25.01	23.99	28.09	15.61	26.42	28.00
7.92	9.96	9.50	7.71	9.13	6.74	6.90	7.11
2.36	2.87	2.38	2.14	2.68	1.85	2.23	1.89
0.91	0.82	0.88	0.86	0.89	0.80	0.89	0.90

11.85	10.29	11.35	12.06	14.44		9.82	9.45	9.19
0.28	0.34	0.26	0.27	0.24		0.21	0.28	0.29

M-127	M-128	*M-10	M-11	*M-14	*M-15	M-19A	M-23
Pillow lavas	*Pillow lavas*	*analcimite*	*analcimite*	*analcimite*	*analcimite*	*analcimite*	*analcime-be*
48.4	49.4	48.9	54.3	47.8	50	50.8	49.4
0.67	0.68	0.86	0.51	0.5	0.54	0.62	0.67
17.2	17.8	17.15	21.1	19.1	19.75	20.2	14.6
7.86	7.83	7.58	3.27	4.37	4.17	4.88	9.16
0.19	0.2	0.19	0.21	0.12	0.19	0.19	0.17
3.61	3.87	3.92	1.07	1.61	2.61	1.72	5.68
6.7	6.39	4.7	2.75	4.43	2.89	4.57	7.09
4.58	4.24	6.29	6.41	7.3	7.17	5.99	6.43
3.69	4.23	2.32	5.76	1.84	4.52	4.94	1.19
0.56	0.56	0.69	0.17	0.38	0.28	0.43	0.45
0.35	0.29	0.17	0.23	0.15	0.26	0.24	0.11
4.83	4.88	6.8	4.95	9.33	8.56	5.31	4.17
98.79	100.67	99.69	100.99	97.09	100.98	100.25	99.14
14.70	14.00	11.44	0.81	2.75	3.34	5.31	112.63
268.76	254.45	292.55	123.28	111.42	161.89	217.31	333.48
16.20	15.43	11.82	3.32	4.85	3.62	6.29	83.50
22.57	22.40	16.64	5.36	8.61	8.36	10.97	31.00
6.89	6.76	6.66	0.38	2.00	1.98	2.48	21.50
116.16	122.68	211.34	28.18	45.85	65.64	159.41	69.52
89.88	92.96	150.13	102.53	70.75	89.58	99.15	146.13
67.64	81.87	44.24	65.02	28.57	81.52	82.06	72.80
1990.06	2191.69	1045.36	2121.78	1082.35	682.67	3038.98	1363.92
24.11	24.43	31.22	26.97	19.56	23.66	24.92	43.16
107.28	110.43	172.87	215.03	206.10	160.64	181.33	104.46
8.43	8.55	15.78	23.94	20.09	15.48	21.59	11.03
1.17	0.68	0.84	0.98	0.74	0.37	1.19	0.43
0.92	0.92	1.17	1.25		1.11	0.98	1.75
2.53	3.26	2.23	2.24	4.48	3.95	1.59	13.77
3074.79	2532.71	1395.30	1978.21	1194.32	2198.64	2128.32	1801.40
28.65	28.97	49.44	55.53	37.71	43.84	47.73	29.96
52.47	53.60	91.42	97.74	65.90	78.08	84.23	53.04
6.37	6.68	10.81	10.57	7.34	8.74	9.38	6.53
26.23	26.70	43.13	37.11	27.05	32.61	35.05	26.67
5.56	5.49	8.65	6.64	4.93	6.08	6.90	6.03
1.55	1.64	2.35	1.91	1.30	1.84	1.93	1.74
5.28	5.35	7.55	5.84	3.36	5.44	5.71	6.36
0.73	0.73	0.99	0.85	0.57	0.74	0.77	0.95
4.00	4.13	5.19	4.47	3.12	4.02	4.18	5.73
0.81	0.79	1.05	0.91	0.63	0.79	0.81	1.20
2.29	2.28	2.88	2.53	1.82	2.03	2.15	3.33
2.16	2.17	2.49	2.54	1.89	2.13	2.18	3.35
0.32	0.33	0.39	0.39	0.30	0.32	0.31	0.51
2.49	2.62	3.62	4.28	3.19	3.20	3.42	2.99
0.49	0.52	0.63	1.17	1.06	0.74	0.98	1.33
1.31	1.14	0.48	1.30	2.48	1.64	0.78	0.45
27.34	28.14	20.63	43.32	21.69	30.94	43.00	18.16
7.37	7.40	10.77	15.05	14.42	11.25	13.11	23.10
2.19	2.17	2.79	4.89	5.13	3.25	4.44	1.22
0.87	0.92	0.89	0.94	0.98	0.98	0.94	0.86

9.50	9.56	14.24	15.66	14.32	14.74	15.73	6.41
0.28	0.28	0.31	0.42	0.51	0.34	0.44	0.35

M-24	M-33	M-35	Ditection limit	Reference Materials	
				BE-N (measured)	BE-N (GeoRem)
analcime-be	*analcime-be*	*analcime-bearing lavas*			
49.4	47.9	58.3			
0.56	0.85	0.61			
19.3	17.35	16.65			
6.11	7.72	5.84			
0.17	0.22	0.11			
2.4	2.93	2.73			
6.11	6.75	5.35			
3.47	5.02	4.11			
5.78	3.56	2.94			
0.52	0.6	0.34			
0.23	0.21	0.12			
5.17	4.29	3.14			
99.39	97.65	100.35			
6.88	13.92	10.05	-	23.79	22.55
200.37	282.13	104.99	0.278	239.40	231.9
7.55	14.35	22.49	1.56	358.03	353.1
15.82	19.17	13.38	0.113	60.76	59
3.26	6.06	7.99	22.2	266.93	269.7
164.77	141.44	16.71	2.02	68.84	68.8
82.80	104.20	62.52	74.5	123.79	122.9
98.75	48.67	96.16	0.433	48.99	47.61
1791.35	2225.75	747.47	5.32	1422.17	1392
19.83	29.83	25.70	-	31.35	29.44
102.35	170.70	136.91	1.38	289.48	272.9
8.71	19.87	21.38	1.71	119.13	113.2
0.35	2.53	1.20	-	2.54	2.75
0.92	1.65	1.30	-	1.97	1.68
2.65	2.38	1.16	0.1	0.85	0.729
1976.98	1793.02	1017.27	20.1	1046.48	1039
29.09	45.51	71.28	0.121	83.22	82.55
52.08	83.84	121.80	0.151	154.68	153
6.09	10.10	12.68	0.04	17.33	17.39
23.52	40.70	44.97	0.084	66.61	66.35
4.61	8.05	7.57	0.078	12.38	12.03
1.40	2.29	2.07	0.065	3.74	3.679
4.32	7.65	6.49	0.259	10.65	10.09
0.56	1.03	0.83	-	1.34	1.303
3.32	5.39	4.60	0.079	6.54	6.48
0.63	1.03	0.84	0.025	1.17	1.084
1.79	2.70	2.34	0.033	2.56	2.605
1.78	2.47	2.11	0.051	1.90	1.817
0.27	0.37	0.30	0.013	0.25	0.2489
2.32	3.73	3.33	1.21	5.44	5.72
0.49	1.07	1.31	0.701	4.87	5.64
0.71	1.44	2.67	-	31.68	28
29.97	30.73	16.41	0.245	4.82	4.081
7.69	10.71	19.90	0.247	10.51	10.58
2.17	2.77	4.36	0.036	2.53	2.44
0.96	0.89	0.90			

11.72	13.19	24.19
0.29	0.42	0.29

DR-N (meas	DR-N (GeoRem)
26.59	20,47-28
213.31	178,28-225
32.10	27-58,6
35.53	9,6-67-2
15.43	11-53,2
43.37	46-82,53
142.50	127,11-177,2
68.50	67,6-141,04
387.54	299,81-440
27.57	18,86-29,16
30.00	107,36-143,7
7.74	4-23,5
0.92	0,83-1,51
2.28	1,84-4,3
5.00	5,96-6,71
379.98	305,96-472
20.54	17,78-52,5
44.01	43,4-46,6
5.39	5,4-5,7
23.18	16,23-23,6
5.18	4,74-5,37
1.41	1,41-1,81
5.10	4,5-11,18
0.79	0,71-0,82
4.58	3,93-4,9
0.96	0,89-1
2.68	2,45-5,06
2.49	2,3-4,35
0.35	0,34-1,73
1.17	2,89-3,56
0.61	0,54-0,64
54.01	132-139
61.63	50,7-62
4.66	4,53-5,06
1.55	1,49-1,69

Table. 2 Isotope composition of the Salavat igneous rocks

Sample No.	Rock type	Rb (ppm)	Sr (ppm)	87Rb/86Sr;	87Sr/86Sr;	ı87Sr/86Sr;	t2se (.10-6)	Sm (ppm)
M-118	*Volcanic breccia*	74.06	298.94	0.69	0.706323	0.70593	29	4.02
M-71	*Lamprophyre*	109.14	617.33	0.49	0.705429	0.70515	12	4.98
M-112	*Lamprophyre*	106.18	609.77	0.49	0.706156	0.70588	10	4.86
M-113	*Lamprophyre*	24.93	756.66	0.09	0.704921	0.70487	12	7.47
CH006B	*Tephrite*	86.90	1038.59	0.23	0.705255	0.70512	13	6.38
M-80	*Tephrite*	93.64	1074.39	0.24	0.705238	0.70510	9	6.92
M-84	*Tephrite*	103.08	1088.91	0.26	0.705561	0.70541	8	7.12
M-47	*Pillow lava*	89.77	1609.59	0.16	0.704725	0.70464	13	4.85
M-128	*Pillow lava*	81.87	2191.69	0.10	0.705143	0.70508	13	5.49

Nd (ppm)	147Sm/144N	143Nd/144N	143Nd/144Nd, t=40 Ma		eNd (40 Ma)
19.50	0.1246	0.512668	0.51264	6	0.8
22.32	0.1348	0.512680	0.51265	5	1.0
24.20	0.1215	0.512622	0.51259	9	0.0
31.32	0.1443	0.512750	0.51271	6	2.3
30.50	0.1265	0.512662	0.51263	8	0.7
32.09	0.1305	0.512684	0.51265	7	1.1
32.61	0.1320	0.512601	0.51257	13	-0.5
23.65	0.1240	0.512804	0.51277	5	3.5
26.70	0.1243	0.512788	0.51276	7	3.2